Trends in C_1-C_4 Alcohol Oxidation Activity Enhancement for Tunable Silicon Oxide Encapsulated Platinum Electrocatalysts

Marissa E.S. Beatty,[1] Marlee Herring,[1] Nicole H. Llewellyn,[1] Lucas A. Cohen,[1] Alexis T. Haley,[1]

Zhexi Lin,[1] Miguel A. Modestino,[2] Daniel V. Esposito[1,]*

[1]Columbia University in the City of New York

Department of Chemical Engineering

Columbia Electrochemical Energy Center

Lenfest Center for Sustainable Energy

500 W. 120th St., New York, NY 10027

[2]New York University

Department of Chemical Engineering

6 Metrotech Center, Brooklyn, NY, 11201

***Corresponding author**
E-mail: de2300@columbia.edu
Phone: 212-854-2648

Abstract

Electrooxidation of carbon monoxide (CO) and small oxygenate molecules is of great interest for direct alcohol fuel cell (DAFC) and electroorganic synthesis. Herein, we demonstrate that carbon-modified silicon oxide (SiO_xC_y) overlayers with nanoscopic thickness can greatly enhance the activity of Pt electrodes towards the oxidation of CO and five different oxygenate molecules. Trends in activity are reported with respect to the composition and structure of the SiO_xC_y overlayers, revealing that low-density, carbon-rich overlayers enhance peak current densities towards the oxidation of formic acid, methanol, ethanol, 1-propanol, and 1-butanol by 370%, 290%, 190%, 130%, and 30%, respectively, compared to bare Pt controls. Unlike conventional alloy electrocatalysts, the alcohol oxidation activity of SiO_xC_y|Pt electrodes did not strongly correlate with their ability to oxidize CO intermediates, suggesting that that C-H bond scission and/or oxidation of aldehyde or carboxylic acid intermediates, rather than CO intermediates, are the rate limiting steps during the oxidation of C_1 and C_2 alcohols. For larger alcohols like propanol and butanol, oxidation activity on encapsulated electrodes diminishes relative to bare Pt, which is attributed to mass transport limitations introduced by the overlayer. Overall, the structure-property-performance relationships uncovered in this study provide new insights into how overlayers can alter reaction mechanisms and can be used to guide design of encapsulated catalysts for alcohol oxidation and electroorganic synthesis reactions.

Key words: electrocatalysis, direct alcohol fuel cells, buried interface, overlayer, alcohol oxidation, carbon monoxide oxidation, platinum, silicon oxide

I. Introduction

Electrochemical alcohol oxidation reactions (AORs) have been extensively studied for their relevance to direct alcohol fuel cells (DAFCs), which utilize energy-dense alcohol fuels like methanol and ethanol for energy conversion.[1] However, the efficiencies and power densities of DAFCs lag behind those of hydrogen fuel cells,[2] which limits their end-use applications. Research efforts aimed at improving DAFC performance have primarily focused on improving the durability, selectivity, and activity of the anode electrocatalysts towards AORs. One challenge that is often cited as a barrier to increasing AOR activity is the fact that carbon monoxide (CO), a commonly observed reaction intermediate, is a poison for many platinum-based catalysts.[3] Besides possessing high tolerance to CO and activity towards O-H and C-H bond cleavage, electrocatalysts designed for oxidizing alcohols with two or more carbon atoms (C_2+) must also be able to efficiently cleave C-C bonds, which is necessary for complete conversion to CO_2.[4] To address the CO poisoning issue, researchers have explored different catalyst geometries,[5,6] co-operative catalyst schemes,[7,8] and alternative support materials[9] that are capable of decreasing the CO bond strength of active sites, and ease its removal at lower potentials. Some progress has also been made in the development of electrocatalysts for the oxidation of C_2+ alcohols like ethanol,[10,11] mainly through the use of Rh-based alloys that can facilitate C-C bond scission. However, the performance of these electrocatalysts still lags behind the best electrocatalysts used for oxidation of C_1 alcohols.

One approach towards improving the performance of alcohol oxidation electrocatalysts is to encapsulate the active electrocatalyst with an ultrathin (< 10 nm) oxide overlayer. Previous work on such oxide-encapsulated electrocatalysts (OECs) by Takenaka[12] and Robinson[13] has demonstrated that silicon oxide (SiO_x) overlayers deposited on Pt electrocatalysts can substantially increase the current densities associated with methanol oxidation. CO stripping voltammetry experiments in the latter study revealed that the presence of SiO_x decreased the onset potential for CO oxidation by 100-180 mV compared to bare Pt, indicating that the SiO_x overlayer may reduce the binding energy of CO located at the SiO_x|Pt buried interface. Takenaka *et al.* also explored the use of SiO_2|Pt electrocatalysts for ethanol oxidation,[12] but in contrast to the results for methanol, the SiO_2 overlayers showed decreased ethanol oxidation reaction activity compared to bare Pt. These studies demonstrated that encapsulating Pt electrocatalysts within oxide layers can strongly influence their ability to oxidize small organic molecules. However, a mechanistic understanding of how the chemical and physical properties of these oxide overlayers impacts alcohol oxidation activity does not exist. A major challenge towards gaining such understanding is that there are multiple different mechanisms by which overlayers could be affecting AOR performance at the buried catalytic interface. An example of the different types of mechanisms by which overlayers might influence oxidation of alcohols (R-OH) are illustrated in Figure 1, including (i.) assisted removal of adsorbed CO intermediates by a reactive overlayer (Fig. 1a), (ii.) confinement effects that favor reaction pathways through reactive (i.e. non-poisoning) intermediates (Fig. 1b), (iii.) selective rejection of competitive spectator anions (Fig. 1c), and (iv.) reactant/product transport limitations (Fig. 1d).

As illustrated in Figure 1a, overlayers may alter reaction pathways by being directly involved in the reaction mechanism. For example, Robinson *et al.* hypothesized that SiO_x overlayers can provide proximal Si–OH groups to co-react with adsorbed CO intermediates at the SiO_x|Pt buried interface and thereby enhance methanol oxidation activity.[13] Overlayers may also influence reaction kinetics indirectly by imposing steric confinement effects that stabilize certain intermediates, or destabilize others.[14] The decreased solubility of supporting electrolyte anions,

which are known to affect AOR activitiy,[15,16] within SiO_x overlayers may also indirectly impact AOR kinetics. Finally, as the overlayer composition is altered, so too can its transport properties towards products and reactants. As species fluxes to/from the surface may be restricted by the introduction of an overlayer, products can accumulate at the buried interface during AOR, leading to large concentration overpotentials and/or pH differentials with implications for electrode efficiency and stability.

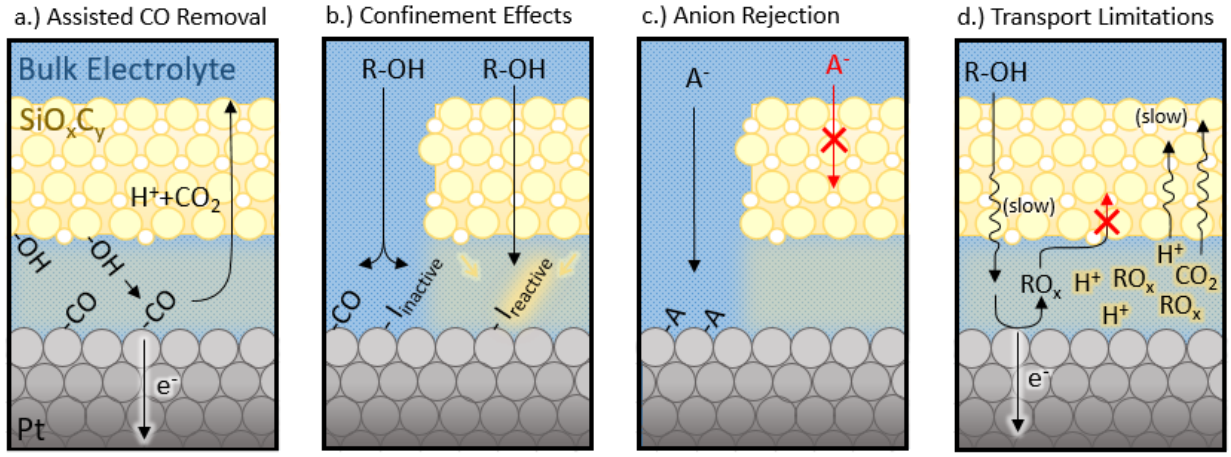

Figure 1. Summary of possible mechanisms by which a SiO_xC_y overlayer may impact the activity of encapsulated Pt active sites towards the oxidation of alcohols (R-OH). a.) Silanol-assisted CO removal. b.) Stabilization and promotion of the formation of more active surface intermediates (labelled "$I_{reactive}$") relative to stable surface intermediates (labeled "$I_{inactive}$") c.) Rejection of anionic species (A^-) that may reduce the coverage of active sites for alcohol oxidation. d.) Suppressed transport of alcohol species to active sites at the buried interface and slow removal of intermediates (RO_x) and products (H^+, CO_2) that result in large concentration gradients between the bulk electrolyte and buried interface. Note: Images are not drawn to scale. The gap between the overlayer and the catalyst is exaggerated to illustrate elementary processes occurring at the buried interface.

With these hypotheses in mind, a major objective of the current study was to better understand the mechanistic origins of the enhanced alcohol oxidation activity of SiO_x-encapsulated Pt electrocatalysts. To this end, a two-pronged approach was taken. First, all experiments were based on planar thin-film Pt electrocatalysts using a photochemical deposition process that affords excellent control over the thickness, composition, and density of the resulting carbon-modified silicon oxide (SiO_xC_y) overlayers.[17] Planar SiO_xC_y|Pt thin film electrocatalysts were used to (i.) eliminate the role of structure-sensitive reactivity associated with Pt nanoparticles or other high surface area Pt structures, (ii.) ensure a well-defined active surface area from sample to sample, and (iii.) allow for comparison with previous studies that used similar planar electrodes. A second objective of this study was to expand the analysis of SiO_xC_y|Pt electrodes to a broader range of small organic molecules than those studied previously – specifically including CO, formic acid, methanol, ethanol, 1- and 2-propanol, and 1- and 2-butanol. As the oxidation of many of those molecules can involve the same or similar intermediates, comparing the similarities and differences in their oxidation behavior on SiO_xC_y|Pt electrodes presents an opportunity to establish empirical trends between performance metrics, overlayer characteristics, and reactant properties. This approach has previously been employed by Herrero *et al.* to help uncover similarities and differences in rate limiting steps for bare Pt electrodes towards oxidation of a series of C_1 and C_2 intermediates.[18]

Using the methodology outlined above, this study reports the AOR performance of well-defined SiO_xC_y|Pt electrodes containing SiO_xC_y overlayers with thicknesses of 4.4 nm - 7.2 nm and carbon content of 5 at. % - 30 at. %. After describing synthesis procedures and physical characterization of SiO_xC_y|Pt electrodes, cyclic voltammetry carried out in 0.5 M H_2SO_4 and 0.5 M $HClO_4$ supporting electrolytes is used to analyze the influence of overlayer characteristics on electrochemically active surface area and Pt oxide formation features. Next, the electrocatalytic performances of SiO_xC_y|Pt electrodes towards the oxidation of C_1 molecules (carbon monoxide, formic acid, and methanol) and C_2+ molecules (ethanol, propanol, and butanol) are presented, and trends in AOR activity with respect to overlayer and alcohol characteristics are analyzed. Lastly, the discussion section explores the origins of AOR activity enhancement resulting from oxide encapsulation.

II. Materials and Procedures

Monocrystalline degenerately doped $p^+Si(100)$ wafers (Prime-grade p^+Si, resistivity <0.005 Ω cm, 500–550 μm thick, WRS materials) were used as conductive substrates. 2 nm of titanium (Ti) and 50 nm of Pt at 99.9% purity were sequentially deposited by electron-beam deposition under high vacuum ($< 5 \times 10^{-8}$ Torr) at rates of 0.5 and 1 Å s^{-1}, respectively. The deposited wafers were then washed sequentially in acetone, methanol, isopropanol, and deionized water. A solution of high-molecular-weight trimethyl siloxy-terminated poly(dimethylsiloxane) (PDMS, 28000 Da, Gelest Inc.) in toluene (2.8 mg mL^{-1}) was spin-coated onto the Pt|Ti|p^+Si substrates for 2.5 min at 4000 rpm. The PDMS-coated electrodes were then dried under vacuum (25 in. Hg) at 90 °C for 1 hr. before undergoing treatment in a UV–ozone chamber (UVOCS, T10X10/OES) to convert the PDMS to SiO_xC_y. Replicate samples were fabricated in all cases.

Electrodes were cleaved into two identical "sister" samples, with one used as a control sample for background CVs, and the other used for CVs carried out in the presence of the oxygenate molecule of interest. SiO_xC_y overlayer thicknesses were measured using a J.A. Woollam α-SE ellipsometer. The thicknesses of SiO_xC_y overlayers in the SiO_x|Pt|Ti|p^+Si samples were determined by sequentially fitting the raw data using a Cauchy model with optical constants derived for SiO_2 (n = 1.44) and substrate thicknesses determined from fitting bare control samples lacking SiO_xC_y overlayers. Electrical contacts were attached by soldering a copper wire onto the back of the silicon substrate with indium solder using a soldering iron temperature of 218 °C. The geometric area of the electrode was defined using 3M electroplater's tape, resulting in a circular 0.246 cm^2 opening through which the electrocatalytic surface was exposed to the electrolyte. Samples were characterized using scanning electron microscopy (Zeiss Sigma VP SEM), atomic force microscopy (Bruker Dimension Icon AFM, ScanAsyst silicon nitride tip) and X-ray photoelectron spectroscopy (Phi 5500, Al Kα source, $<10^{-7}$ Torr) as described elsewhere[17,19] to ensure that prepared overlayers were uniform in thickness and composition.

All electrolytes were prepared using 18 MΩ deionized water (Millipore, Milli-Q Direct 8). 0.5 M sulfuric acid and perchloric acid supporting electrolyte solutions were prepared from concentrated H_2SO_4 (Certified ACS plus, Fischer Scientific) and $HClO_4$ (Sigma-Aldrich, Certified ACS/NF), respectively. These solutions both yielded a pH of 0.29. All electrochemical measurements were carried out using a SP-200 BioLogic potentiostat and conducted in a round-bottom glass cell at ambient temperature (≈ 25 ° C) with a commercial Ag|AgCl (3 M KCl) reference electrode (Hach, E21M002, $E°$ = 0.21 V vs normal hydrogen electrode (NHE)) and a carbon rod (Saturn Industries) counter electrode. All electrolytes were deaerated by purging with

nitrogen gas (N_2, UHP) for 20 min. Prior to all measurements, electrodes were conditioned by performing cyclic voltammetry (CV) in the supporting electrolyte for 10 cycles between 0.05 and 1.20 V vs. RHE at 100 mV s^{-1}. Background CVs were obtained by analyzing the sister sample under identical conditions used for alcohol oxidation CVs. All reported current densities were normalized by the geometric area of the exposed electrode.

For CO stripping measurements, a background CV was taken starting from 0.2 V vs RHE, and cycling to 0.05 and 1.2 V vs. RHE for 4 cycles. Next, CO gas was vigorously bubbled into solution at a flow rate of > 1.0 L min^{-1} while applying a 0.05 V vs. RHE bias to the electrode. The CO was switched off after 10 minutes, and the solution was purged with N_2 for 30 minutes at a flow rate of 1 L min^{-1} to remove dissolved CO. A CV was taken immediately following the CA, without returning to open circuit voltage between measurements. CVs were initiated at 0.2 V vs. RHE, just below the oxidation potential of CO, and swept negative to 0.05 V vs. RHE to characterize the hydrogen underpotential deposition (H_{upd}) features. Using the same potential vertices as the control experiment, three additional cycles were taken – the first to define CO stripping behavior, and the following to confirm the complete removal of adsorbed CO and absence of signal from the oxidation of dissolved CO in the bulk electrolyte.

Alcohol oxidation CV measurements began by conditioning all samples with 10 CV cycles taken in 0.5 M sulfuric acid supporting electrolyte as described above. Next, formic acid (ACROS Organics, >99%), methanol (CH_3OH, Fisher Chemical, ACS grade), ethanol (Decon Laboratories Inc., Anhydrous, >99.5%), 1-/2- propanol (Sigma-Aldrich, ≥ 99.7%), or 1-/2- butanol (Sigma-Aldrich, ≥99.5%) were added to set the oxygenate concentration at 0.5 M. CVs were initiated at the lowest potential vertex of 0.05 V vs. RHE and swept at a scan rate of 100 mV s^{-1} to an upper potential vertex of 1.2 V vs. RHE, except in the case of butanol, which requires an upper potential vertex of 1.4 V vs. RHE to decompose on Pt. CV cycling was carried out until a steady state voltammogram (i.e. one that does not show >1% difference between cycles) was obtained – approximately 35 cycles.

AOR gaseous product quantification was measured during extended (650 – 850 cycles) CV cycling of OEC electrodes. CVs were swept from a lower vertex potential of 0.35 V vs. RHE at a scan rate of 100 mV s^{-1} to an upper vertex potential of 1.2 V vs. RHE. Evolved gases were collected using a sealed H-type electrochemical cell (DEK Research, CHR221B2) shown in Figure S9, which allowed controlled placement of a planar working electrode with an exposed area of 2.55 cm^2, a carbon rod counter electrode, and a miniature Ag|AgCl reference electrode (3 M KCl, $E°$ = 0.21 V vs NHE, eDAQ, ET073-3) in an airtight chamber. The working electrode chamber was separated from the counter electrode chamber by a Nafion membrane (Nafion 212, Fuel Cell Store, 593263), and each chamber of the cell contained 30 mL of electrolyte plus 15 mL of gas headspace. N_2 at 1 sccm, regulated by a mass flow controller (Masterflex, EW-32907-57), flowed through the headspace during alcohol oxidation and was injected into a gas chromatograph (SRI 8610C, Multi-Gas #5 Configuration) via an automated sample loop in 1 mL aliquots. Samples were taken every 25-30 minutes until a steady state gas composition (< 10% difference between samples) was obtained – approximately 3 – 5 samples. Representative chromatograms from experimental runs and for control solutions are provided in Figure S12. Faradaic efficiencies were calculated from gaseous product compositions measured over 3 successive injections, with full details provided in Supporting Information Section IV.

AOR liquid product quantification was carried out using nuclear magnetic resonance (NMR) spectroscopy. NMR samples were prepared by adding 50 µL of dimethyl sulfone (98%, Sigma Aldrich) as an internal standard to a mixture of 500 µL of electrolyte from the working electrode compartment and 100 µL of D_2O (99.9% atom % D, 1% w/w 3-(trimethylsilyl)-1-propanesulfonic acid, sodium salt (DSS), Sigma Aldrich). ^{1}H NMR (Bruker 400SL MHz) spectra were obtained using a 15 µs excitation pulse length averaged over 16 repetitions with a 1 s delay between acquisitions. ^{13}C NMR spectra (Bruker 500 MHz) were obtained using a 9.750 µs excitation pulse length averaged over 40,000 repetitions with a 1 s delay between acquisitions.

III. Results and Discussion

3.1 Electrode Preparation and Characterization

Platinum thin film electrodes encapsulated by 4.4 nm – 7.2 nm thick carbon-modified silicon oxide (SiO_xC_y) overlayers were prepared and characterized as described elsewhere.[17] Briefly, SiO_xC_y overlayers were fabricated following a room-temperature photochemical conversion process for which an ultraviolet-ozone (UV-Ozone) chamber was used to convert a poly-dimethyl siloxane (PDMS) precursor into silicon oxide (SiO_x) through reaction between reactive oxygen species and the PDMS. Previous studies have detailed how varying the time of this UV-Ozone curing step affects the density and amount of residual carbon left within the final SiO_xC_y film.[17,20] Curing times of 120 minutes or more have been found to result in dense SiO_2-like overlayers with low carbon content (< 6 at. %).[17,21] As curing times beyond 120 minutes had little additional impact on overlayer structure or composition, SiO_xC_y overlayers cured for 120 minutes are considered to be "fully cured". Meanwhile, "partially cured" samples subjected to ≤ 60 minutes contain 10 at. % – 20 at. % carbon and densities that were 10% – 40% lower than the fully cured samples. The SiO_xC_y|Pt electrodes used in the current study have been previously characterized using X-ray photoelectron spectroscopy (XPS), scanning electron microscopy (SEM), atomic force microscopy (AFM), and ellipsometry.[17] Characterization results for each sample are provided in the Supplemental Information (Figures S1 & S2) and summarized in Table I.

Table I. Physical and chemical properties of SiO_xC_y| overlayers deposited on Pt thin film electrodes. *†Relative concentrations and compositions calculated from XPS data.*

Curing time	Thickness	Carbon content†	O:Si†	Density
min	nm	at %	-	g cm^{-3}
30	6.8 ± 0.4	20.6	2.34	1.70 ± 0.04
60	5.1 ± 0.3	8.0	2.88	2.17 ± 0.07
90	5.0 ± 0.3	5.4	2.63	2.32 ± 0.04
120	4.7 ± 0.3	5.4	2.06	2.54 ± 0.04

Before carrying out AOR experiments, CVs were taken in 0.5 M H_2SO_4 (Figure 2) or 0.5 M $HClO_4$ (Figures S4) supporting electrolytes to investigate the influence of overlayers on the electrochemically active surface area (ECSA) of the buried Pt sites and view how anion identity affects the ability of Pt to form Pt hydroxides (Pt-OH) and oxides (PtO_x). Since surface oxide/hydroxides can be involved as co-reactants in CO and alcohol oxidation, differences in oxidation behavior of Pt caused by the presence of an overlayer can be expected to impact alcohol oxidation behavior as well. A bare Pt control electrode subjected to 120 minutes of curing was also

included to disentangle the effects of surface cleaning caused by UV curing on CV characteristics from influence(s) of the SiO_xC_y overlayer (Figure S3). In Figure 2, the CV curve for the bare Pt electrode displays the familiar hydrogen underpotential deposition (H_{upd}) features at low potentials (0.05 – 0.4 V vs. RHE) and Pt oxidation and reduction features at higher potentials (0.6 – 1.2 V vs. RHE) that are characteristic of polycrystalline Pt.[16]

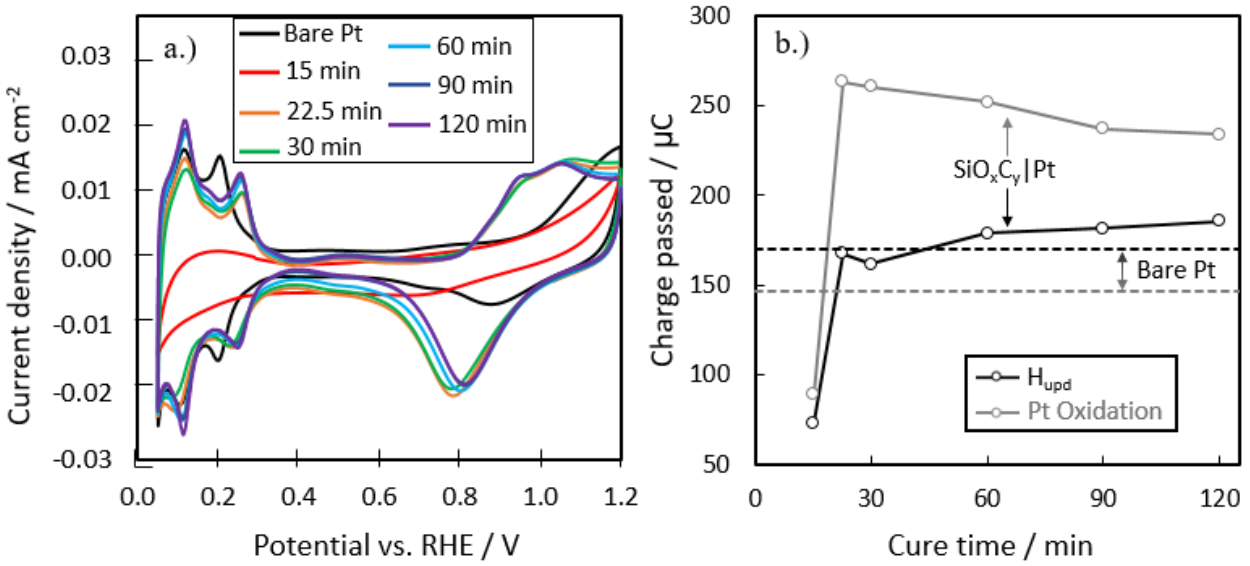

Figure 2. a.) Cyclic voltammograms of samples of varying UV-ozone curing times (t_{cure}) cycled between 0.05 V and 1.25 V vs. RHE until steady state behavior was reached, showing the 20th cycle for measurements taken in 0.5 M sulfuric acid electrolyte at 10 mV s^{-1}. b.) Integrated charge for the hydrogen underpotential deposition (0 – 0.4 V) and Pt oxidation (0.6 - 1.2 V) regions of the CV from a.) for bare Pt (dashed lines) and SiO_xC_y|Pt (solid lines) electrodes each electrode.

Analyzing the H_{upd} regions of the CV curves in Figure 2a reveals that there are no significant losses in ECSA following encapsulation, meaning that the SiO_xC_y overlayers are not blocking H^+ from reaching buried Pt sites. As shown in Figure S3, the UV-Ozone treatment of the bare Pt electrode was also not found to have a statistically significant influence on H_{upd}, Pt oxidation, or methanol oxidation features. In contrast, significant differences in PtO_x features are observed when comparing CVs for bare Pt and SiO_xC_y|Pt. While the onset of Pt oxidation to Pt-OH (Equation 1) for bare Pt electrode is located at ≈ 0.9 V vs. RHE, consistent with literature,[22,23] this onset shifts by ≈ -100 mV for all SiO_xC_y|Pt electrodes except that cured for 15 minutes. The ability of SiO_x overlayers to shift the Pt oxidation onset potential to more negative potentials has been previously reported[19,24] and attributed to the overlayer's ability to suppress adsorption of sulfate anions to the Pt surface that can delay the formation of Pt oxides until sulfate desorption at higher potentials.[25,26]

$$H_2O + Pt \rightarrow e^- + H^+ + Pt - OH \quad (1)$$

To further confirm this effect, CV measurements were also taken in 0.5 M perchloric acid, which contains weakly binding chlorate anions that do not greatly suppress Pt oxidation.[27] As seen in Figures S4 and S5, these CVs reveal that the onset of Pt oxidation is slightly less positive (≈ 50 mV) for encapsulated electrodes compared to bare Pt (Figure S4). By comparing the differences in Pt oxidation onset potential between sulfuric and perchloric acid electrolytes, it can be inferred

that the overlayers are capable of suppressing sulfates from reaching the buried Pt interface to some degree.

As seen in Figure 2b, the H_{upd} and Pt oxidation features for the SiO_xC_y|Pt sample with the shortest curing time (t_{cure} = 15 min.) were substantially different from all other samples. While samples subjected to longer curing times exhibited negligible changes in overlayer thickness after CV cycling, ellipsometry measurements of the t_{cure} = 15 min. sample revealed that the overlayer thickness decreased by > 95%. For this reason, the t_{cure} = 15 min. electrodes were left out of further investigations, and an additional, intermediate cure time (t_{cure} = 22.5 min.) was included. This t_{cure} = 22.5 min. electrode demonstrated similar PtO_x and H_{upd} regions to all of the longer cured samples. As seen in Figure 2b, all SiO_xC_y|Pt electrodes with curing times > 15 min. possess H_{upd}-derived ECSAs that are very similar to bare Pt but have integrated Pt oxidation signal that exceeds that of Pt by 60% – 80% in the 0.5 M H_2SO_4 supporting electrolyte, credited again to the suppression of competitive anion binding.

3.2 Carbon Monoxide Oxidation Reaction

Next, carbon monoxide (CO) stripping voltammetry was performed for SiO_xC_y|Pt electrodes to establish how the onset potential for CO oxidation is affected by overlayer composition (Figure 3a). As shown in Equation (2), electrooxidation of CO involves the transfer of 2 electrons and the formation of an additional C=O bond:

$$CO + H_2O \rightarrow CO_2 + 2H^+ + 2e^- \quad (2)$$

Since the removal of adsorbed CO intermediates is often believed to be the rate limiting step for the complete oxidation of alcohol to CO_2 at potentials lower than that required for PtO_x formation (≈ 0.8 V vs. RHE),[28,29] the onset and peak potentials for CO oxidation recorded in CO stripping voltammetry experiments are frequently used as descriptors of overall oxidation activity for AOR catalysts. Following initial conditioning CVs in supporting electrolyte, as-made samples were held at a potential of 0.05 V vs. RHE in 0.5 M sulfuric acid for 10 minutes under constant CO bubbling to allow CO to diffuse through the overlayers and adsorb to the buried Pt surface. After purging the solution with N_2 to remove dissolved CO from the bulk electrolyte, CV cycling was initiated by sweeping the potential from 0.2 V vs. RHE to a negative scan vertex of 0.05 V vs. RHE to view H_{upd} signal. Across all samples, it is seen that there is almost no (< 0.01 mA cm^{-2}) current observed for the H_{upd} region, indicating that nearly all available Pt sites are initially occupied by CO at the start of the scan, and that CO is able to permeate through the SiO_xC_y overlayers during the preceding CO purge step. After reaching the negative scan vertex, the electrode potential was swept towards positive potentials to oxidize the adsorbed CO to CO_2. In Figure 3, clear peaks associated with CO oxidation are observed at potentials greater than 0.6 V vs. RHE for all samples. For bare Pt, a majority of the total stripping current is contributed by the peak at ≈ 0.80 V vs. RHE, consistent with values previously reported for CO removal on polycrystalline Pt.[30] For the encapsulated samples, the primary CO stripping peak shifts to less positive potentials, with the CV curves for all $t_{cure} \geq 60$ min. overlayers showing a major peak at 0.70 V vs. RHE and minor peaks around 0.68 and 0.51 V vs. RHE. The encapsulated samples also share a CO oxidation peak at 0.76 V vs. RHE, which is most pronounced for the t_{cure} = 30 min. sample and gradually diminishes as curing time is increased.

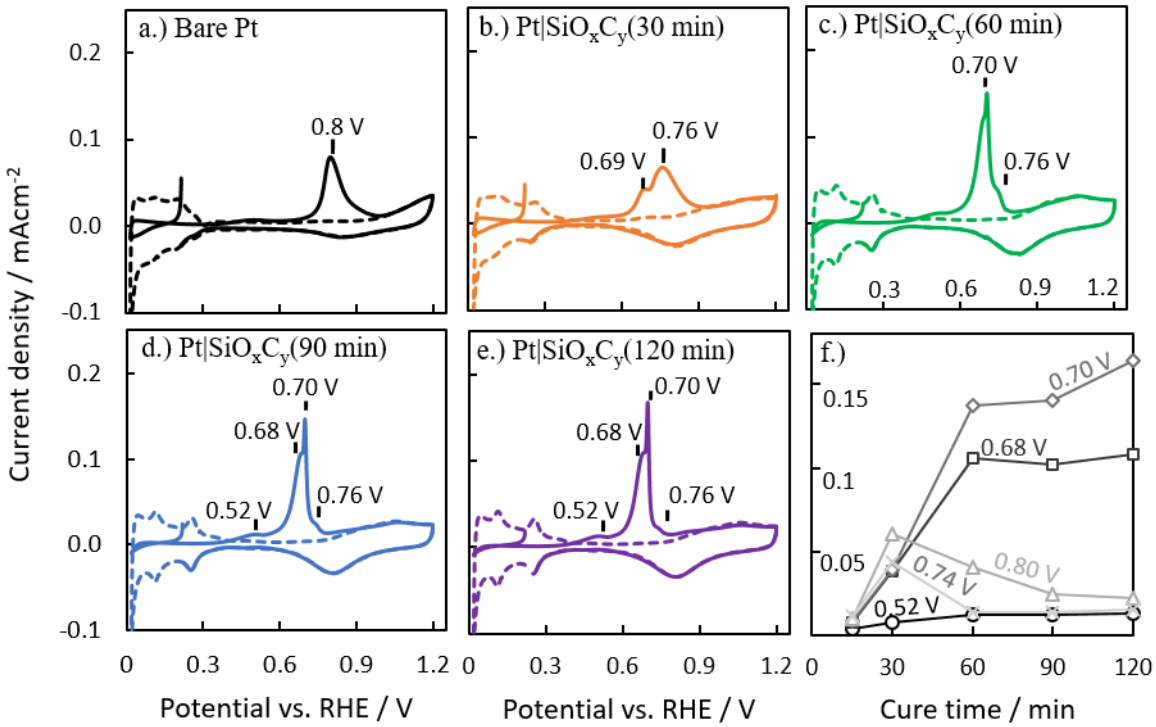

Figure 3. (a. – e.) CO stripping voltammograms of samples of varying UV-ozone curing times (t_{cure}) in N_2 purged 0.5 M H_2SO_4 electrolyte following CO purging at +0.05 V vs. RHE. Dashed lines depict the 2nd CV following the initial first cycle of CO stripping at 10 mV s^{-1}. f.) CO oxidation current density at five discrete potentials as a function of electrode curing time.

3.3 Formic Acid Oxidation Reaction (FAO)

Another intermediate of methanol oxidation on Pt electrodes is formic acid,[31] which is also of interest as a fuel itself.[32] The complete oxidation of formic acid to CO_2 requires C-H scission, O-H scission, and C=O formation steps, while involving the transfer of two electrons:

$$HCOOH \rightarrow CO_2 + 2H^+ + 2e^- \quad (3)$$

There are two main pathways through which the FAO reaction proceeds on Pt,[33,34] as illustrated in Figure 4a: (i.) a direct pathway that forms a surface formate (COOH) intermediate that can be further oxidized to CO_2, and (ii.) an indirect pathway that forms a poisoning CO intermediate before proceeding to CO_2 at higher potentials. In the direct (formate) pathway, the FAO reaction may proceed through the monodentate (C-H down formate) or bidentate (OO down formate) configuration. Recent experimental and density functional theory (DFT) studies of formic acid oxidation have shown that the monodentate intermediate can rapidly proceed to CO_2, but the bidentate orientation is inactive for the complete oxidation to CO_2 due to the inaccessibility of the C-H bond to the active surface, making C-H bond cleavage the rate limiting step.[35–37]

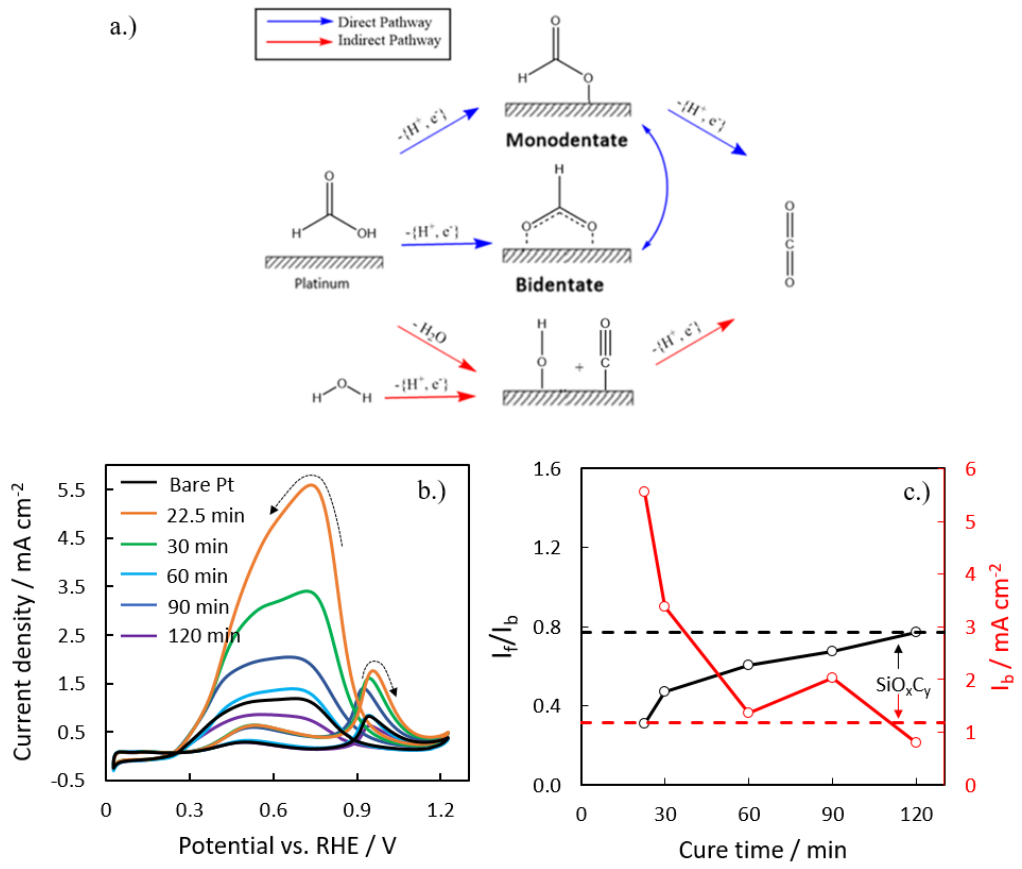

Figure 4. a.) Reaction pathways for formic acid oxidation demonstrating the direct, active formate intermediate pathway (in blue), and indirect, poisoning pathway (in red). b.) Cyclic voltammograms (35th cycle) for bare Pt and SiO_xC_y|Pt electrodes of varying UV-ozone curing times recorded in 0.5 M formic acid + 0.5 M sulfuric acid electrolyte at 100 mV s^{-1}.c.) Dependence of the backward scan peak current density (I_b) and ratio of the forward peak current density (I_f) to I_b on cure time. Dashed lines represent the values measured for a bare Pt control electrode.

CV cycling of bare Pt in 0.5 M formic acid + 0.5 M H_2SO_4 (Figure 4b) results in a well-known CV profile on bare Pt that has oxidation peaks in both the forward (positive-going) and backward (negative-going) scans. The first peak in the forward scan is attributed to the decomposition of formic acid into adsorbed formate and CO intermediates.[38] As the potential is increased beyond 0.6 V vs. RHE, the current subsides as intermediates accumulate on the catalyst surface and block active sites. At potentials > 0.8 V vs. RHE, Pt-OH groups form and react with CO and/or formate intermediates to generate the peak at ≈ 0.95 V vs. RHE. As the potential is increased beyond 1.0 V vs. RHE, the Pt surface becomes saturated with Pt–OH and Pt oxides, which reduces current once more. Upon reversing the scan direction, a second major oxidation peak emerges at potentials < 0.75 V vs. RHE, where the PtO_x species formed during the forward scan are reduced and free up sites for alcohol decomposition.

Also shown in Figure 4b are representative CV cycles for SiO_xC_y|Pt electrodes recorded under identical conditions. These CVs exhibit the same features as the bare Pt electrode, but the magnitudes and peak locations vary depending on the overlayer cure time. Comparing to the CV curves for bare Pt, those for the encapsulated samples show increased peak current density for FAO during both the forward and backwards scans, with the magnitude of the forward peak for the fully cured SiO_xC_y|Pt electrode being the only exception. The greatest differences in current

densities are observed for the peaks recorded during the backward (reverse) scan of the CV between 0.8 V and 0.25 V vs. RHE, designated as "I_b". As shown in Figures 4c and S5a, the SiO_xC_y|Pt electrodes with the shortest curing times demonstrated the highest current density enhancement, with the t_{cure} = 22.5 min. electrode achieving > 360% in I_b compared to bare Pt. The peak center locations for oxidation peaks in the positive scan direction are similar for all electrodes, while a skew to positive potentials is seen in the backward scan oxidation peaks for the low cure time SiO_xC_y|Pt electrodes.

Because of the integral role of Pt-OH species during oxidation of small organic molecules like formic acid, the hysteresis between the forward and backwards peaks (I_f and I_b, respectively) has been used as a common descriptor of catalyst oxophilicity, or how easily a catalyst can form surface hydroxyls.[39,40] In general, CV curves for more oxophilic catalysts are expected to be characterized by a higher I_f/I_b ratio, while those for less oxophilic catalysts exhibit a lower I_f/I_b ratio. Figure 4c shows the I_f/I_b ratios for bare Pt (dashed black line) and encapsulated electrodes as a function of cure time (solid black line). While shorter cure time samples display much lower I_f/I_b values than the bare Pt, this ratio monotonically increases with cure time until the fully cured electrodes have ratios that are very similar to bare Pt.

3.4 Methanol Oxidation Reaction (MOR)

The next oxygenate molecule investigated was methanol, for which complete oxidation to CO_2 requires the cleavage of three C-H bonds and one O-H bond while forming two C=O bonds through a total of six electron transfers:

$$CH_3OH + H_2O \rightarrow CO_2 + 6H^+ + 6e^- \quad (4)$$

The MOR contains many of the same elementary reactions steps as the two electron FAO reaction, but involves a more complex reaction network as shown in Figure 5a. As with FAO, the rate of the MOR is generally known to be limited by removal of strongly bound intermediates and to follow a dual-pathway mechanism that forms either an active formate intermediate that can be fully oxidized to CO_2 at low potentials,[41] or a CO intermediate that poisons the surface and delays oxidation until the formation of adsorbed hydroxyls.[42,43] Though these reactions share many similarities, a distinction between them is that methanol oxidation requires an additional C-H cleavage and C=O formation step for its complete oxidation to CO_2.[44] Another difference is that the complete oxidation of methanol, unlike FAO, involves consumption of H_2O as a co-reactant.

CV curves for Pt and SiO_xC_y|Pt electrodes measured in 0.5 M CH_3OH + 0.5 M H_2SO_4 are provided in Figure 5b. For all samples, the general features appearing in these CV curves are similar to those seen in the CV curves measured in 0.5 M CHOOH, but with a couple differences. First, bare Pt displays very low MOR activity below the onset of Pt oxidation at ≈ 0.8 V vs. RHE due to CO poisoning.[45] Second, the backward peak for MOR is much narrower than that of FAO, which can be largely attributed to the +220 mV shift in the standard reduction potential for methanol compared to formic acid. As seen in Figure 5c, SiO_xC_y|Pt electrodes demonstrate the same trend of increasing peak current density (I_b) with decreasing curing time that was seen for FAO, but with all encapsulated samples showing greater oxidation activity than bare Pt. The fully cured (t_{cure} = 120 min) SiO_x layer shows a ≈ 30% increase in I_f compared to bare Pt, in contrast to the FAO CV in Figure 4b where the fully cured SiO_xC_y|Pt sample displayed similar I_f to bare Pt. Once again, the t_{cure} = 22.5 min. SiO_xC_y|Pt electrode was the most active, with a maximum enhancement of ≈ 70% for I_f, and ≈ 290% for I_b (Figure S6b). When comparing relative

performances, it is also notable that I_b for the t_{cure} = 22.5 min electrode is only a factor of 2.1 larger than that of the t_{cure} = 120 min electrode for MOR, compared to a factor of 4.7 observed during FAO.

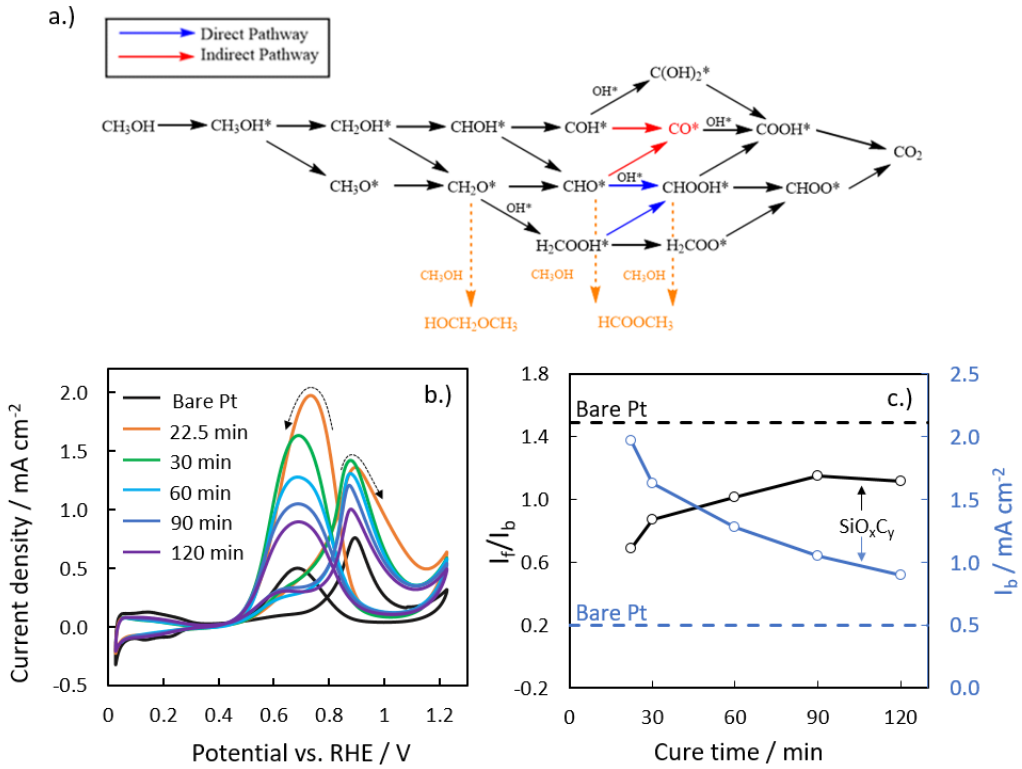

Figure 5. a.) Reaction scheme for methanol oxidation based on that proposed by Wang, et. al. in ref. [43] b.) Cyclic voltammograms (35th cycle) of bare Pt and SiO_xC_y|Pt electrodes of varying UV-ozone curing times (t_{cure}) recorded in 0.5 M methanol + 0.5 M H_2SO_4 at 100 mV s^{-1}. Dashed arrows indicate scan direction. c.) Dependence of the magnitude of the backward scan peak current density (I_b) and ratio of the forward peak current density (I_f) to I_b on overlayer cure time. Dashed lines represent the values measured for a bare Pt control electrode.

Given that both the MOR and FAO have similar reaction mechanisms and common rate limiting steps, it is to be expected that the overlayer cure time might have similar effects on activity and I_f/I_b ratios recorded in CV curves for both molecules. Indeed, when comparing plots of I_f/I_b vs. cure time in Figures 4c and 5c, the same trend for the MOR and FAO emerges. SiO_xC_y|Pt electrodes undergoing shorter curing times were characterized by smaller I_f/I_b ratios compared to those measured for electrodes that underwent longer curing times.

3.5 C_2+ Alcohol Oxidation

Oxidation reactions of larger C_2+ alcohols like ethanol, propanol, and butanol are also of great interest for DAFC applications since these molecules are less toxic, less flammable, and have higher energy densities than methanol and formic acid.[29,46] However, unlike the oxidation of formic acid and methanol, the complete oxidation of C_2+ alcohols to CO_2 requires efficient cleavage of C-C bonds. Such C_2+ alcohols also require more co-reactant H_2O molecules and total electron transfers to achieve complete oxidation to CO_2, as seen in Equation (5a). Two possible reactions associated with incomplete oxidation of ethanol are also provided in Equations (5b-c):

Complete Oxidation: $CH_3CH_2OH + 3H_2O \rightarrow 2CO_2 + 12H^+ + 12e^-$ (5a)

Incomplete Oxidation: $CH_3CH_2OH + H_2O \rightarrow CH_3COOH + 4H^+ + 4e^-$ (5b)

$CH_3CH_2OH + H_2O \rightarrow CH_3COH + 2H^+ + 2e^-$ (5c)

To evaluate the impacts of overlayers on C_2+ alcohol oxidation, CV measurements were carried out in 0.5 M ethanol, 1- and 2-propanol, and 1- and 2-butanol solutions for bare Pt and SiO_xC_y|Pt electrodes with cure times of 30 min., 60 min., and 120 min. Representative CV curves in the ethanol solution are provided in Figure 6a. The ethanol oxidation reaction follows a similar parallel pathway reaction scheme to those described above for formic acid and methanol oxidation, forming either oxygen-bound ethoxy intermediates that can yield various non-CO_2 products and poisoning intermediates, or carbon-bound oxygenate intermediates that can directly progress to CO_2.[47] Because these competing pathways contain many of the same (or similar) dehydrogenation steps and poisoning intermediates as the MOR and FAO, CV profiles for ethanol oxidation are also characterized by separate oxidation peaks in both the forward and backwards scans. As seen in Figure 6a, the location of the oxidation peak in the forward scan is centered around 1.0 V vs. RHE for all samples. This location is more positive than the locations of the oxidation peaks seen in Figures 4b and 5b for FAO and MOR, respectively, and has been attributed to the larger kinetic overpotential required to oxidize adsorbed C_2 intermediates like acetate and acetic acid compared to CO and formate/formic acid.[4]

Ethanol oxidation CVs display the same trends in I_f vs. overlayer cure time that were seen for formic acid and methanol oxidation, where the electrodes subjected to the shortest cure times display the largest I_f values – up to 190% higher than bare Pt. However, peak current densities during the backward scan do not show the same degree of enhancement relative to bare Pt (up to 80% higher) that was observed for partially cured SiO_xC_y|Pt electrodes tested for MOR (up to 290% higher) and FAO (up to 370% higher). Additionally, the location of the EOR peaks in the backwards scan are shifted to more positive potentials than bare Pt sample by up to ≈ 90 mV. Notably, the t_{cure} = 30 min sample is the only electrode that exceeds the activity of the bare Pt sample for the backwards scan, with the longer cure times resulting in a decrease in I_b.

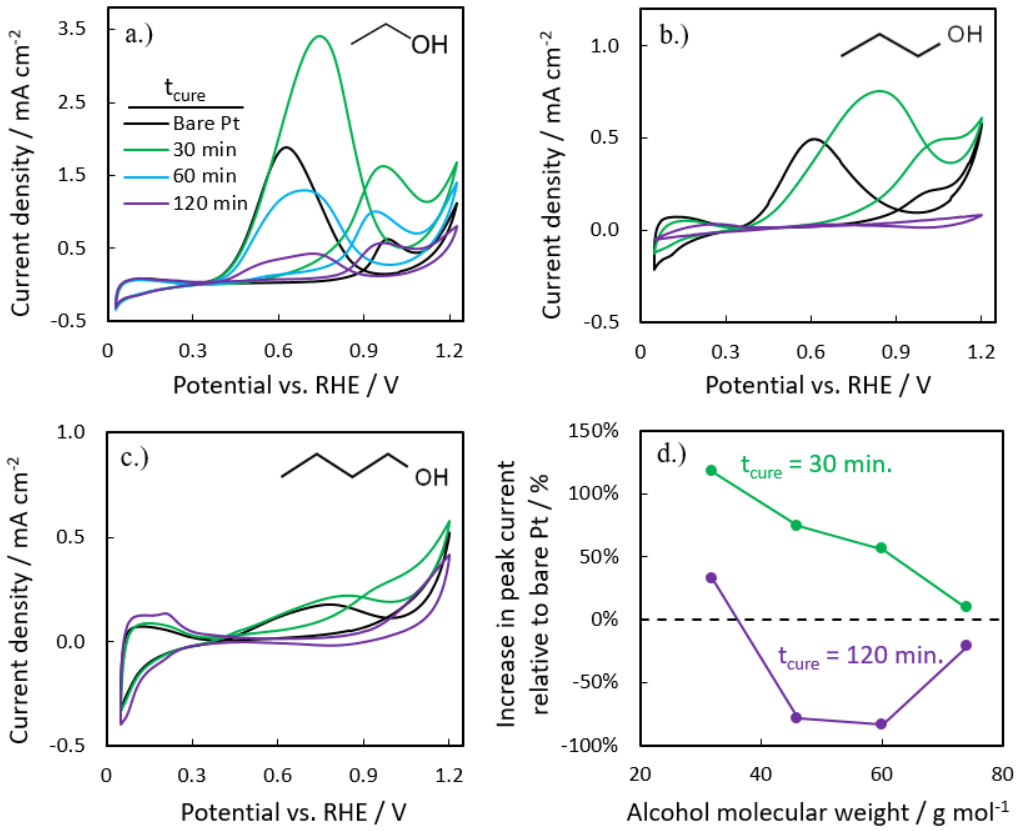

Figure 6. CV curves for bare Pt and SiOxCy|Pt electrodes recorded in a.) 0.5 M ethanol, b.) 0.5 M 1-propanol, and c.) 0.5 M 1-butanol. Representative CV curves recorded during the 40th cycle are shown, and were measured using a scan rate of 100 mV s^{-1} in a 0.5 M H_2SO_4 supporting electrolyte. d.) Summary of the percent increase in maximum alcohol oxidation current density for samples with partially and fully cured overlayers, compared to the maximum current density for a bare Pt electrode and plotted as a function of alcohol molecular weight.

Representative CV curves for SiO_xC_y|Pt and bare Pt electrodes are also shown for 1-propanol and 1-butanol in Figure 6b and 6c, respectively. As seen in Equations (6) and (7), complete oxidation of 1-propanol and 1-butanol involves 18 and 24 electrons per alcohol, with additional C-C bond scission steps beyond what is required for ethanol.

$$CH_3C_2H_4OH + 5H_2O \rightarrow 3CO_2 + 18H^+ + 18e^- \quad (6)$$

$$CH_3C_3H_6OH + 7H_2O \rightarrow 4CO_2 + 24H^+ + 24e^- \quad (7)$$

Inspection of oxidation features in Figure 6b shows that the same trend of activity enhancement vs. overlayer cure time is seen for the 1-propanol oxidation reaction (1-POR) that was noted for ethanol. The t_{cure} = 30 min. electrode displays peak current densities that are increased by factors of 2.3 and 1.5 relative to bare Pt for the forward/backward sweeps, respectively. The t_{cure}= 120 min. sample shows almost no observable current for 1-POR. A similar positive potential shift for the backward peak location is seen again for the t_{cure} = 30 min. SiO_xC_y|Pt electrode during 1-propanol oxidation, but is much larger than the shift seen for the EOR, such that the backward peak for the t_{cure} = 30 min. electrode is positioned ≈ 230 mV more positive than that for bare Pt.

The largest alcohol investigated in this study was 1-butanol, for which representative CV curves for SiO_xC_y|Pt and bare Pt samples are provided in Figure 6c for 0.5 M 1-butanol + 0.5 M H_2SO_4. These curves show a significant decrease in current densities for all electrodes compared to all other oxygenates investigated. Furthermore, the encapsulated electrodes achieve the lowest degree of activity enhancement over bare Pt compared to the results shown in Figures 2-6b. This is evident by viewing the percent increase in the maximum peak current signal as a function of molecular weight for all primary alcohols studied in this work (Figure 6d). The t_{cure} = 120 min. sample shows almost no activity at all for the 1-butanol oxidation reaction (1-BOR) beyond its background measured in supporting electrolyte (Figure S8). Given that this sample displays the largest integrated H_{upd} area during butanol oxidation, it is likely that the losses in activity are due to the mass transport constraints imposed by the dense SiO_2-like overlayer, rather than the formation of poisoning intermediates, which would reduce H_{upd} signal. This observation, along with the negligible oxidation signal seen in Figure 6c for the 120 min. SiO_xC_y|Pt electrode, suggests that the 1-BOR current density is suppressed by the ability of the larger 1-butanol molecule to reach the buried interface.

3.6 Analysis of Liquid and Gaseous Products

Online gas chromatography (GC) measurements were used to analyze the impact of the presence and curing time (t_{cure} = 30 or 120 min.) of the SiO_xC_y overlayer on the ability of the SiO_xC_y|Pt electrode to completely oxidize alcohols to CO_2. Additionally, NMR was used to quantify liquid phase MOR products by analyzing electrolyte sampled after the completion of CV cycling. Methanol and ethanol were chosen as representative C_1 and C_2 species for which sufficiently high reaction rates towards AOR were observed during CV cycling to allow for the detection of CO_2 by online GC or NMR. A detailed description of the procedures for GC experiments can be found in Section SIV of the Supporting Information. Briefly, gas products were periodically sampled from the headspace of an H-cell while carrying out CV cycling between 0.35 V and 1.20 V vs. RHE. The faradaic efficiency for the complete oxidation of alcohol to CO_2 (FE_{CO2}) was calculated using the measured production rate of CO_2 relative to the theoretical maximum, which was determined by Faraday's law based on the total charge passed during the gas sampling window. It should be noted that the MOR and EOR pathways are potential dependent, and the results from this analysis are an average or blended result of the product species evolved over the entire potential window used for CV measurements.

Results of MOR product analysis are provided in Figure S11 for bare Pt, 30 min. SiO_xC_y|Pt, and 120 min. SiO_xC_y|Pt electrodes. The FE_{CO2} for bare Pt was 36.4 ± 8.9% for methanol, closely matching previously reported results for polycrystalline Pt.[48,49] The other primary product detected during MOR on bare Pt was methyl formate (FE_{MF} = 63.6 ± 5.0%), which results from reaction of methanol with formic acid, an incomplete oxidation product from MOR that has been frequently reported in literature.[50–52] Meanwhile, electrodes based on partially (t_{cure} = 30 min.) and fully (t_{cure} = 120 min.) cured SiO_xC_y overlayers demonstrated FE_{CO2} of 37.0 ± 6.7% and 86.7% ± 4.7%, respectively. While no other product could be detected for the fully-cured SiO_xC_y|Pt electrode besides CO_2, significant amounts of liquid-phase methoxymethanol (MM), a 2 e^- transfer product, were observed by NMR for the partially-cured SiO_xC_y|Pt electrodes (FE_{MM} =59.4 ± 4.3%). Methoxymethanol has been previously detected by NMR as an MOR product,[52,53] and is believed to form from the reaction of formaldehyde intermediates with methanol,[53] as shown in Figure 5a.

When online GC measurements were carried out for an identical set of samples during CV cycling in 0.5 M ethanol, all three electrodes exhibited similar low conversion rates to CO_2, with FE_{CO2} varying between 1 – 4 % (Figure S13). These results indicate that neither the partially nor fully cured SiO_xC_y overlayers promote the cleavage of C-C bonds required to form CO_2 during ethanol oxidation on Pt catalysts. Besides CO_2, the other significant gas-phase product was acetaldehyde, which was detected for all electrodes and is consistent with previous reports of acetaldehyde generation during ethanol oxidation on Pt.[10,54]

IV. Discussion

This study revealed several trends between the properties of silicon oxide encapsulated Pt electrocatalysts and their performance towards alcohol oxidation. Most notably, SiO_xC_y|Pt electrodes based on shorter curing times (C-rich SiO_xC_y) displayed even greater activity enhancement towards MOR than previous studies that used longer curing time SiO_2-like overlayers,[12,13] and showed that the oxidation of larger C_2+ alcohols was not only possible, but even promoted on some encapsulated electrodes compared to bare Pt. For nearly all alcohol oxidation reactions, encapsulation with a lower-density, carbon-rich SiO_xC_y overlayer increased the peak current densities compared to bare Pt, while the denser, SiO_2-like overlayers achieved higher activity than bare Pt for all but the C_2+ alcohols. Additionally, analysis of MOR products reveals that the presence and composition of oxide overlayers can alter the dominant reaction pathway(s) for alcohol oxidation. Together, these observations motivate the questions: (i.) by what mechanism(s) do overlayers increase alcohol oxidation activity, (ii.) why do the carbon-rich overlayers outperform the carbon-deficient overlayers, and (iii.) how can the answers to these questions be used to guide the design of encapsulated catalysts that maximize alcohol oxidation activity and selectivity towards a target product species? Due to the number of confounding factors that can influence AOR performance, this discussion section is organized into sub-sections that explore the relevance and merit of each of the proposed mechanisms illustrated in Figure 1.

4.1 Overlayer-Assisted CO Removal

One of the most common approaches to improving AOR activity on Pt-based catalysts is to modify the catalyst surface in a way that decreases the potential required to oxidize CO, which is commonly achieved by alloying Pt with a more easily oxidized metal, like ruthenium or tin.[55,56] These less noble metals promote the formation of nearby metal hydroxide (M–OH) groups at lower potentials than pure Pt, which assist in the removal of CO through the so-called bi-functional mechanism.[55,57,58] Thus, comparing the results from this study with those observed from Pt-alloys can help determine if the improvements in AOR activity are the result of improved hydroxyl formation and subsequent CO removal.

Alloying Pt with oxophilic metals produces two major effects on CV curves used to characterize AOR reactions: i.) it increases the current density associated with alcohol oxidation and ii.) it increases the I_f/I_b ratio.[39] It follows that traditional Ru- or Sn-alloyed Pt electrocatalysts tend to display increases in alcohol oxidation activity that correlate with a decrease in CO oxidation overpotential as well as decreased onset potentials for surface oxidation in supporting electrolyte. However, the SiO_xC_y|Pt electrodes studied in this work did not display these same correlations. For example, while the long cure time SiO_xC_y|Pt electrocatalysts displayed the largest decrease in CO oxidation overpotential (i.e. $t_{cure} \geq 90$ min) and largest I_f/I_b ratios, they displayed the *lowest* degree of activity enhancement for all AORs studied. This observation is most apparent during FAO for the fully cured SiO_x|Pt electrode, which had a CO oxidation peak potential that was 100

mV less positive than that of bare Pt but demonstrated *reduced* FAO activity compared to all other SiO_xC_y|Pt electrodes. The location of the second forward peak (E > 0.8 V vs. RHE) in FAO CVs also did not substantially shift with the onset of CO oxidation, as has been demonstrated on Ru-modified Pt catalysts that promote CO removal at lower applied potentials.[58]

Due to the strong influence of M-OH groups not only on CO removal, but also other steps in AORs, it is important to understand how an overlayer may be perturbing the formation and properties of Pt-OH at the buried interface of an OEC. It can be seen in the CV curves in the 0.5 M sulfuric acid supporting electrolyte (Figure 2) that Pt is oxidized at less positive potentials for SiO_xC_y electrodes compared to bare Pt, which might contribute to decreasing the CO oxidation peak potential. However, all encapsulated samples display similar onset potentials for Pt oxidation, yet oxidize CO at notably different potentials (Figure 3). Thus, although the presence of an overlayer is clearly impacting the ability to remove CO intermediates, it is not likely through promotion of M-OH groups at the buried interface. However, it is notable that the Pt oxidation onset potentials seen in Figure 2 for SiO_xC|Pt electrodes (0.8 – 1.0 V vs. RHE) are still more positive than the CO oxidation onset potentials (0.5 – 0.8 V vs. RHE) observed in Figure 3. For this reason, Robinson *et al.* suggested that the decreased CO oxidation potentials for SiO_x|Pt electrodes may result from interactions between the adsorbed CO and proximal silanol groups (Si-OH) or bridging oxygen species in the SiO_x overlayer, which could potentially serve the same role as Pt-OH in serving as a co-reactant for CO oxidation.[13] This CO removal mechanism could explain the trends seen in Figure 3, where Pt encapsulated by the SiO_2-like, fully cured overlayer exhibits the lowest CO oxidation potential while Pt coated by the carbon-rich, short cure time samples require larger overpotentials to oxidize CO. As these carbon-rich overlayers have fewer $Si\text{-}O^-$ groups available at the buried interface, they would be less likely to facilitate Si-OH-mediated CO removal. By contrast, fully cured electrodes possess SiO_x rich layers that are more likely to contain Si-OH-like species in close proximity to bound CO-Pt at the SiO_x|Pt interface, which may explain the lower CO overpotentials observed for these electrodes.

Regardless of the exact origin of the enhanced CO oxidation activity, the CO oxidation onset potentials in Figure 3 do not correlate with alcohol oxidation activity. This observation suggests that the primary mechanism(s) of activity enhancement by SiO_xC_y|Pt electrocatalysts differs from alloyed electrocatalysts. Since CO removal is the last step in most branches of AOR reaction schemes on Pt at low pH and E < 0.8 V,[10] it is more likely that a different elementary reaction step has become rate determining and that the composition and/or structure of the SiO_xC_y overlayer is impacting its rate as well. Further, it is plausible that improved CO oxidation activity increases the site availability for parallel reactions that subsequently become the new rate determining step over potentials of interest. Since formic acid and methanol both demonstrate the same trends with respect to activity enhancement and I_f/I_b ratios vs. overlayer curing time, this could signify that the new rate determining step is shared between the two reactions. As both molecules can pass through an active formate intermediate,[44] it could be that conversion of oxygen-bound adsorbates containing methoxy or formyl groups dictate overall reaction rate on some of the encapsulated electrodes.

The hypothesis that conversion of other (i.e. non-CO) AOR intermediates determines the overall activity of the SiO_xC_y|Pt electrodes is further supported by analyzing the potentials for which FAO and MOR current densities are maximized. Oxidation peaks appearing at less positive potentials (< 0.8 V vs. RHE) are considered to be limited by the conversion of alcohol reactants to initial intermediates like CO and formate.[38,41] Since these potentials are less than those required

for –OH formation and subsequent CO oxidation, as seen in Figures 2a and 3a, sustained activity in this region can only result from non-CO forming reactions, as has been demonstrated using online product analysis studies for both MOR and FAOR.[59] CO poisoning is evident in the bare Pt CVs recorded in both formic acid (Figure 4b) and methanol (Figure 5b) solutions, which display minimal oxidation current in the forward scans until the potential exceeds ≈ 0.8 V vs. RHE where CO can be oxidized. Unlike the bare Pt electrode, SiO_xC_y electrodes show high activity in regions more negative of the CO oxidation potential. Low cure time electrodes were especially notable for outperforming bare Pt at these potentials. Thus, the enhancement of FAO and MOR activity at lower overpotentials suggests that encapsulated electrodes, especially the low cure time samples, may also be improving the kinetics for steps associated with direct (non-CO) pathways.

4.2 Anion Rejection

Another possible mechanism by which oxide overlayers can influence alcohol oxidation is through their ability to block or suppress supporting electrolyte anions from interfering with Pt oxidation and/or alcohol oxidation steps (Figure 1c). For example, it is well known that sulfate ions can delay the onset of Pt oxidation by adsorbing to the Pt surface.[16] Carrying out CV measurements in both sulfuric acid and perchloric acid electrolytes, for which the weakly bond perchlorate anion does not delay the onset of Pt oxidation,[15,60] offers a means to probe the influence of overlayer-anion interactions on both Pt oxidation and alcohol oxidation activity.[15] Figures S3 and S4 contain CVs in 0.5 M $HClO_4$ for bare Pt and encapsulated electrodes with curing times of 30 and 120 min. A direct comparison of the background CVs in both perchloric acid and sulfuric acid in Figure S5 shows that bare Pt is most sensitive to the introduction of site-blocking (bi)sulfate ions, as the onset of Pt oxidation in perchloric acid is shifted by ≈ -200 mV, consistent with literature.[61] In contrast, the Pt oxidation onset potential for both the fully and partially cured SiO_xC_y|Pt electrodes is decreased by only ≈ -80 mV in perchloric acid, suggesting that the encapsulated electrodes possess similar ability to suppress (bi)sulfate adsorption. The small shift in Pt oxidation onset potentials in the two different electrolytes indicates that (bi)sulfates are still able to access the buried interface of SiO_xC_y|Pt electrodes, albeit to a smaller degree than for bare Pt.

The ability of anions to access and interact with Pt has important implications for site availability and alcohol oxidation kinetics. Previous studies have demonstrated that strongly adsorbing anions such as (bi)sulfate can be advantageous for FAO kinetics by promoting formation of monodentate formate over bidentate formate intermediates by limiting the availability of neighboring Pt sites through competitive adsorption.[37,62,63] However, these strongly bound anions can become detrimental to AOR activity if a catalyst can only facilitate the indirect, poisoning pathway, as their presence on the surface can also suppress formation of surface-bound hydroxyls needed for removal of CO. Analyzing FAO and the MOR in perchloric acid can provide further insight into how differences in site availability caused by changing the identity of the supporting electrolyte anion can alter parallel reaction steps. If rejection of a strongly adsorbing anion species by the overlayer is the primary mechanism of AOR activity enhancement, then it can be expected that switching to a weak-binding anion should decrease or eliminate the difference in activity seen between the encapsulated and bare Pt electrodes.

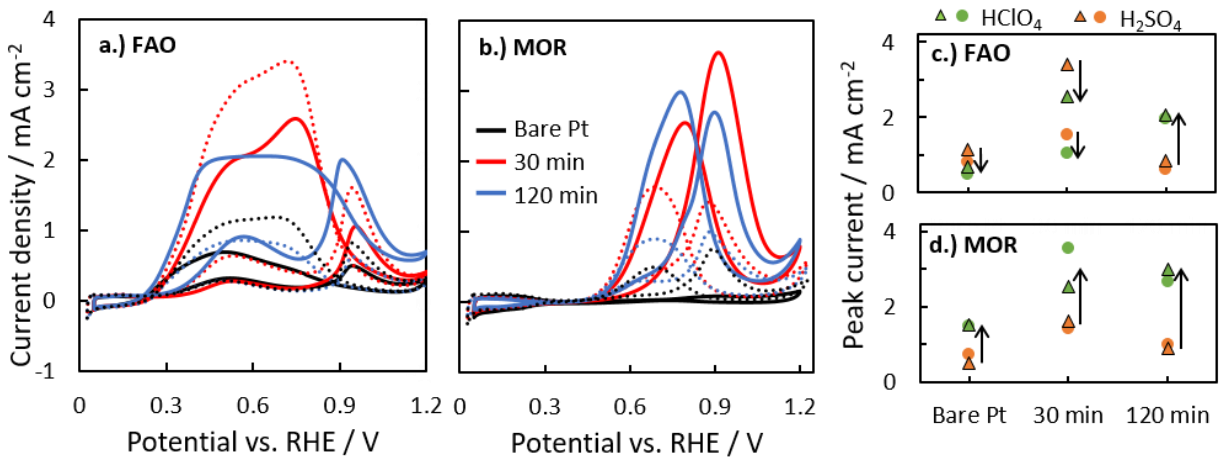

Figure 7. CV curves for Pt and SiO_xC_y|Pt electrodes measured in a.) 0.5 M CHOOH and b.) 0.5 M CH_3OH carried out in 0.5 M $HClO_4$ (solid lines) and 0.5 M H_2SO_4 (dotted lines) at 100 mV s^{-1}. Summaries of the differences in the forward (circle) and backward (triangles) peak current densities measured for each electrode in different supporting electrolytes for FAO and MOR are provided in (c.) and (d.), respectively, where arrows indicate the effect of switching from the H_2SO_4 to $HClO_4$ supporting electrolyte.

As shown in Figure 7a for CVs in 0.5 M formic acid, switching the supporting anion from (bi)sulfate to perchlorate decreased FAO activity for the bare Pt sample in all regions of the CV during FAO. This is consistent with the understanding that the weakly bound perchlorate ions favor formation of the less active (poisoning) bidentate formate intermediate over the more active monodentate intermediate. The t_{cure} = 30 min. sample shows a slight decrease in current density in 0.5 M $HClO_4$ compared to 0.5 M H_2SO_4, but still significantly outperforms bare Pt in the perchloric acid electrolyte, indicating that the enhanced activity of the SiO_xC_y|Pt electrode relative to bare Pt in the H_2SO_4 electrolyte cannot be solely attributed to suppression of competitive (bi)sulfate binding by the overlayer. Interestingly, the t_{cure} =120 min. sample displays an increase in FAO activity when switching to 0.5 M $HClO_4$, which suggests that the fully cured SiO_xC_y|Pt electrodes do not benefit from sulfate-based site competition. Instead, the improved FAO activity for the fully cured SiO_xC_y|Pt sample in 0.5 M $HClO_4$ is consistent with this electrode favoring the CO-forming pathway, which benefits from higher coverage of Pt-OH in the presence of the weakly-adsorbing perchlorate anion.

The AOR activity dependence on anion species was further investigated for MOR, with the recorded CV curves (Figure 7b) showing very different responses to anion identity compared to those seen for FAO. Consistent with previous studies on Pt-based electrocatalysts,[64–67] all Pt and SiO_xC_y|Pt electrodes demonstrated enhanced activity for MOR in 0.5 M $HClO_4$, with the effect being most dramatic for the t_{cure} = 120 min. electrode. This latter result supports the hypothesis that fully cured SiO_xC_y overlayers promote C_1 oxidation through the indirect, CO-mediated oxidation pathway, for which the formation of proximal –OH groups is necessary for removal of CO but hindered by the addition of competitive anions. Meanwhile, the behavior of the partially cured SiO_xC_y|Pt electrodes is more consistent with methanol and formic acid oxidation occurring primarily through a direct pathway that avoids formation of CO intermediates and doesn't strongly depend on the presence of proximal –OH groups. This explanation is further supported by product analysis (Section 3.6) showing that fully-cured SiO_xC_y|Pt electrodes preferentially oxidize methanol into CO_2, while partially-cured SiO_xC_y|Pt electrodes primarily produce

methoxymethanol, an incomplete oxidation product that doesn't involve CO as an intermediate (see Figure 5a).

4.3 Confinement Effects

Overlayers may also affect reaction kinetics by altering the chemical, physical, and/or electronic environment of active sites located at the overlayer/catalyst buried interface.[68] This assertion is well-supported by experimental and theoretical investigations of other confined catalyst architectures that have detailed how the energetics and/or orientation of reactive intermediates can be altered within a confined environment to promote activity or selectivity.[69,70] Other studies have shown that changing the concentration of functional groups in the vicinity of confined active sites can strengthen intermolecular forces like hydrogen bonding in order to promote the formation of intermediates associated with more desirable reaction pathways.[69,71,72] A confined interface can also make smaller reaction intermediates become entropically favored compared to larger, bulkier intermediates that may lose rotational, translational, and/or vibrational degrees of freedom under confinement.[72–74] Based on what is known from other confined catalysis examples, it is likely that differences in SiO_xC_y overlayer density and composition may similarly influence the orientation and/or energetics of surface intermediates during alcohol oxidation.

For the case of FAO on bare Pt, formate intermediates adsorbed in the bidentate configuration are thermodynamically favorable due to their lower adsorption energy compared to monodentate,[75–77] making the former less kinetically active than the latter.[36,77] This idea is corroborated by studies characterizing the distribution of adsorbed formate intermediates on Pt.[78] It is well-established that bidentate intermediates that have the rotational freedom to convert to a monodentate configuration are advantageous for FAO activity.[15,37,75] For lower density, partially cured SiO_xC_y overlayers, we hypothesize that their less compact, "loose" buried interface structure allows some sulfates to be present while promoting facile interconversion between the bidentate and monodentate formate intermediates thanks to a higher degree of spatial and rotational freedom. In contrast, the compact nature of the buried interface between Pt and the dense, fully cured SiO_xC_y overlayer may make it difficult to form the C-H down monodentate intermediate, instead favoring decomposition through the more compact CO or bidentate formate surface intermediates. Taken together, the concept of "loose" and "compact" buried interfaces reinforces the notion that partially-cured SiO_xC_y overlayers promote FAO and MOR through direct (non-CO) pathways while fully cured SiO_xC_y overlayers favor indirect (CO) pathways.

In addition to altering the steric environment at the buried interface, overlayers can also interact with intermediates chemically and electronically. Since formic acid and the alcohol molecules investigated in this work are polar, they can participate in hydrogen bonding with neighboring alcohol or water molecules via their carbonyl (C=O) or alcohol (-OH) groups.[79,80] Thus, the concentration of alcohols, acids, water, or other hydrogen bonding groups within the vicinity of a confined active site could impact the orientation of the oxygenate molecule as it approaches the interface (-OH leading vs. C=O or -CH leading),[80,81] which subsequently influences the identity and orientation of the adsorbate. In this work, fully cured SiO_2-like overlayers can be expected to have well-developed H bond networks associated with Si-O-Si and Si-OH groups.[82] However, partially cured SiO_xC_y overlayers possess methyl groups that are associated with the unreacted organosiloxane precursor[17] and known to exhibit weak H bonding. From this understanding, we surmise that fully cured SiO_2-like overlayers interact with the carbonyl groups of formic acid such that the -OH and -CH groups interact with the Pt surface first, promoting

dehydration to CO. Meanwhile, the methyl-rich partially-cured overlayers that possess weaker hydrogen bonding interactions with carbonyl groups would be expected to more readily interact with the C-H group(s) of oxygenates, leading to delivery of reactants (or intermediates) to the Pt surface in a carbonyl or R-OH first orientation that favors formation of formate or methoxy intermediates.

4.3 Reactant and Product Transport Limitations

For any encapsulated electrocatalyst, it is important to balance the kinetic benefits with mass transport limitations that can limit the local concentration of reactants and/or lead to significantly elevated concentrations of products. A similar trade-off is often observed in meso- and micro-porous materials containing confined catalytic sites, which must also balance kinetic benefits against transport limitations.[83,84] Prior studies of oxide-encapsulated electrocatalysts have modeled transport losses through overlayers,[17,85,86] while others have shown that selective transport properties of overlayers can be leveraged to obtain different concentrations of co-reactive species at a catalyst site to enhance reaction selectivity.[87,88]

For species transport through overlayers, an inverse relationship is expected between species permeability and the size of the diffusing species (i.e. the "permeant"), with small molecules being able to pass more easily through the voids or free volume elements of the overlayer compared to larger, bulkier molecules. For all permeant species that diffuse through void spaces within the overlayer, species permeability can also be expected to vary inversely with overlayer density. These expected relationships are consistent with the observations in Figure 5d, which shows AOR peak current densities for SiO_xC_y|Pt electrodes normalized to those of bare Pt as a function of the molecular weight of each of the primary alcohols investigated. Because the bare Pt electrode is nominally unaffected by transport of alcohols to its surface, and all four alcohols are primary alcohols for which electrooxidation involves similar elementary reaction steps, the trends in normalized current densities plotted in Figure 5d can be expected to be strongly influenced by transport effects introduced by the SiO_xC_y overlayers. For both partially and fully cured SiO_xC_y|Pt electrodes, increasing the size of the alcohol leads to decreases in the peak current densities relative to Pt, consistent with the expectation of lower species permeability with increasing species size. For the partially cured SiO_xC_y|Pt electrodes, the decrease in normalized current density is gradual and monotonic. Meanwhile, the fully cured SiO_xC_y|Pt electrodes exhibit a sharper drop off in normalized current density, which is consistently lower than the low-cure time samples. This observation is not surprising given that the fully cured overlayers are 2.6 times as dense as the low cure time samples (Figure S1) and have previously been reported to greatly limit O_2 transport.[17] Given that the C_{2+} alcohols studied here have much larger kinetic radii (3.8 – 5.0 Å)[89] than O_2 (2.9 Å), it is expected that they would also experience significant transport limitations across SiO_xC_y overlayers having the same density and thickness. As the less dense, partially cured overlayers have a higher void fraction than the fully cured overlayers, it stands to reason that smaller alcohols are able to pass through the low cure time SiO_xC_y overlayers at appreciable fluxes, as evidenced by the significant AOR current densities for methanol and ethanol. While the t_{cure} = 30 min. SiO_xC_y|Pt electrode still achieves higher AOR current densities for C_3 and C_4 alcohols compared to bare Pt (Figure 6 & S15), the degree of enhancement is much lower than for C_1 and C_2 alcohols, suggesting that size of the solvated propanol and butanol molecules are approaching or exceeding the average size of free volume elements within the overlayer.

To further investigate the impacts of mass transport resistance introduced by overlayers on AOR activity, the MOR was studied on SiO_xC_y|Pt electrodes containing overlayers with increased thicknesses (12 – 18 nm). By only changing thickness of the SiO_x layer, the chemical environment at the buried interface remains similar, but there is an increased resistance to the transport of reactants to, and products from, the Pt surface. For both partially and fully cured overlayers, increasing overlayer thickness decreased peak current densities by 26 – 68 % and shifted the forward scan peak by ≈ 100 – 20 mV compared to the thinner overlayers, respectively (Figure S9). However, this decrease in peak current density was much more substantial on the fully cured electrode (-68%) compared to the partially cured electrode (-26%). These results are consistent with simple 1-dimensional transport models,[68] which state that mass transfer limiting current densities across overlayers should vary inversely with overlayer thickness. At all thicknesses, the partially cured electrodes still presented higher activities than fully cured overlayers for all alcohol molecules investigated, agreeing with the expectation that the lower density overlayers should enable higher species permeabilities than the high density overlayers.

In addition to impacting transport of the reactant oxygenate molecule to the buried active sites, overlayers can also affect the local concentration of product species like H^+ by suppressing their diffusion away from the buried interface. Previous work has shown that fully cured, SiO_x-like overlayers possess H^+ permeabilities 2-3 orders of magnitude greater than partially cured, PDMS-like overlayers.[17] Given that protons are produced through multiple surface dehydrogenation steps (*i.e.* O-H and C-H cleavage) during AORs, overlayers with low H^+ permeability are expected to lead to a local decrease in pH at the buried interface, and subsequently decrease AOR activity.[15,90] Thus, the partially cured overlayers characterized by low H^+ permeability should show poorer kinetics if significant buildup of H^+ were occurring. However, this relationship is not observed in this study, as the partially cured overlayers that are most likely to lead to local acidification show the highest activity. Further, when looking at the progression of CV cycles for standard thickness (≈ 5 nm) SiO_xC_y|Pt electrodes over time, there is no decrease in peak current densities or observable change to the reaction onset potential that would suggest an imposed Nernstian shift caused by concentration overpotentials (Figure S7). By contrast, thicker (10 – 15 nm) partially cured overlayers did show a positive shift in the MOR peaks as overlayer thickness increased. Thus, local acidification at the buried interface cannot be ruled out for thicker (> 10 nm) SiO_xC_y overlayers.

Besides affecting transport of the oxygenate reactant and H^+, overlayers may also impact transport of co-reactants (i.e. H_2O) and/or intermediates produced during alcohol oxidation between the buried interface and the bulk electrolyte. One possible consequence of suppressed egress of an intermediate like formaldehyde or formate is that it may experience a longer residence time at the buried interface than it would for a bare Pt electrode. This would result in a higher local concentration of the intermediate(s) at the buried interface, increasing the statistical probably that additional reaction steps involving these species are promoted. GC results presented in Section 3.6 are consistent with this idea. For example, the dense, fully cured SiO_xC_y|Pt electrode displays nearly a 2-fold increase in the faradaic efficiency of methanol to CO_2 compared to either bare Pt or the lower density, low-cure time SiO_xC_y|Pt. Although the role of H_2O transport is often ignored in conventional electrocatalysis due to its high concentration (55 M for pure H_2O), it is possible that lowered activity of H_2O caused by the hydrophobic C-rich SiO_xC_y overlayers may also impact the observed results since H_2O is the co-reactant required for complete conversion of methanol to CO_2. Consistent with this explanation, the more hydrophobic low cure time SiO_xC_y|Pt electrodes

exhibit a high faradaic efficiency towards an incomplete reaction product (methoxymethanol) while the long cure time SiO_xC_y|Pt electrodes containing hydrophilic (water loving) SiO_2 overlayers achieve the highest faradaic efficiency towards the complete reaction product (CO_2). Further support for the idea that the hydrophobic character of SiO_xC_y layers can affect branching ratios is seen in the CO_2 reduction literature, where researchers have shown that polymer encapsulation layers strongly influence product distribution.[91–93] Thus, the influence of the hydrophilic character of oxide overlayers on H_2O activity at the buried interface, and subsequently the branching ratio between different alcohol oxidation reaction pathways, is a topic that warrants further exploration.

V. Conclusions

This study investigated the performance of SiO_xC_y -encapsulated Pt electrocatalysts towards CO oxidation and a series of alcohol oxidation reactions (AORs) as a function of SiO_xC_y overlayer composition and structure. It was found that thin (4 – 7 nm thick) SiO_xC_y overlayers were able to improve the activity of SiO_xC_y|Pt electrocatalysts towards all 6 of the investigated molecules compared to bare Pt electrodes. For all alcohol oxidation reactions, the highest performing electrodes were those based on partially-cured overlayers, which are characterized by lower density and higher carbon content than their fully cured counterparts. During CV cycling, the partially cured SiO_xC_y|Pt electrodes gave peak current densities that were 370%, 290%, 190%, 130%, and 30% higher than those for bare Pt control samples in formic acid, methanol, ethanol, 1-propanol, and 1-butanol, respectively. The monotonic decrease in enhancement with alcohol size was attributed to increasing transport limitations of the overlayer. Fully cured SiO_2-like overlayers also exhibited enhanced activity towards methanol oxidation, but showed lower activity than bare Pt for all other reactions. Despite displaying lower formic acid and alcohol oxidation activity than the partially-cured electrodes, the fully-cured electrodes displayed the lowest overpotential (highest activity) for electrooxidation of CO, a commonly observed intermediate in the oxidation of formic acid and alcohol molecules. This observation counters conventional explanations regarding AOR enhancement by Pt alloy catalysts for which reduced CO binding energy is strongly correlated with improved AOR activity. The poor correlation between AOR activity and CO oxidation activity indicates that CO oxidation is not the rate determining step for SiO_xC_y|Pt electrocatalysts over potential ranges of interest for DAFCs, suggesting that other elementary steps like C-H or O-H bond cleavage are rate determining. Additionally, electroanalytical measurements and product analysis provide evidence that the fully cured SiO_2-like overlayers promote small molecule oxidation through indirect (CO-mediated) pathways that favor conversion to CO_2, while the partially cured SiO_xC_y overlayers favor partial oxidation of small molecules through direct (non-CO) pathways. Regardless of the underlying mechanisms that explain these effects, the present study highlights the exciting opportunities for using tunable oxide overlayers to alter complex electrochemical pathways without needing to modify the composition of the underlying catalyst. It is expected that these findings, when combined with further experimental and theoretical investigations, will support the rational design of OEC architectures for a large number of electrochemical reactions involving organic molecules.

VI. Acknowledgements

This material is based upon work supported by the National Science Foundation under Grant Number (CBET-1752340). Any opinions, findings, and conclusions or recommendations expressed in this material are those of the author(s) and do not necessarily reflect the views of the

National Science Foundation. N.L., D.E., and M.M. would also like to acknowledge the Alfred P. Sloan Foundation for supporting this work (Grant #201-16807) that is part of the Center for Decarbonizing Chemical Manufacturing Using Sustainable Electrification (DC-MUSE). N.L. acknowledges support from the Columbia University Bridge to the Ph.D. Program.

VII. References

(1) Fadzillah, D. M.; Kamarudin, S. K.; Zainoodin, M. A.; Masdar, M. S. Critical Challenges in the System Development of Direct Alcohol Fuel Cells as Portable Power Supplies: An Overview. *Int. J. Hydrogen Energy* **2019**, *44* (5), 3031–3054. https://doi.org/10.1016/j.ijhydene.2018.11.089.

(2) Chen, Y.; Bellini, M.; Bevilacqua, M.; Fornasiero, P.; Lavacchi, A.; Miller, H. A.; Wang, L.; Vizza, F. Direct Alcohol Fuel Cells: Toward the Power Densities of Hydrogen-Fed Proton Exchange Membrane Fuel Cells. *ChemSusChem* **2015**, *8* (3), 524–533. https://doi.org/10.1002/cssc.201402999.

(3) Kakati, N.; Maiti, J.; Lee, S. H.; Jee, S. H.; Viswanathan, B.; Yoon, Y. S. Anode Catalysts for Direct Methanol Fuel Cells in Acidic Media: Do We Have Any Alternative for Pt or Pt–Ru? *Chem. Rev.* **2014**, *114* (24), 12397–12429. https://doi.org/10.1021/CR400389F.

(4) Ferre-Vilaplana, A.; Buso-Rogero, C.; Feliu, J. M.; Herrero, E. Cleavage of the C-C Bond in the Ethanol Oxidation Reaction on Platinum. Insight from Experiments and Calculations. *J. Phys. Chem. C* **2016**, *120* (21), 11590–11597. https://doi.org/10.1021/acs.jpcc.6b03117.

(5) Cui, C. H.; Li, H. H.; Yu, S. H. Large Scale Restructuring of Porous Pt-Ni Nanoparticle Tubes for Methanol Oxidation: A Highly Reactive, Stable, and Restorable Fuel Cell Catalyst. *Chem. Sci.* **2011**, *2* (8), 1611–1614. https://doi.org/10.1039/c1sc00233c.

(6) Mazzotta, E.; Caroli, A.; Pennetta, A.; De Benedetto, G. E.; Primiceri, E.; Monteduro, A. G.; Maruccio, G.; Malitesta, C. Facile Synthesis of 3D Flower-like Pt Nanostructures on Polypyrrole Nanowire Matrix for Enhanced Methanol Oxidation. *RSC Adv.* **2018**, *8* (19), 10367–10375. https://doi.org/10.1039/c7ra13269g.

(7) Rafiee, M.; Miles, K. C.; Stahl, S. S. Electrocatalytic Alcohol Oxidation with TEMPO and Bicyclic Nitroxyl Derivatives: Driving Force Trumps Steric Effects. *J. Am. Chem. Soc.* **2015**, *137* (46), 14751–14757. https://doi.org/10.1021/jacs.5b09672.

(8) Gerken, J. B.; Stahl, S. S. High-Potential Electrocatalytic O2 Reduction with Nitroxyl/NOx Mediators: Implications for Fuel Cells and Aerobic Oxidation Catalysis. *ACS Cent. Sci.* **2015**, *1* (5), 234–243. https://doi.org/10.1021/acscentsci.5b00163.

(9) Ramli, Z. A. C.; Kamarudin, S. K. Platinum-Based Catalysts on Various Carbon Supports and Conducting Polymers for Direct Methanol Fuel Cell Applications: A Review. *Nanoscale Res. Lett.* **2018**, *13*. https://doi.org/10.1186/s11671-018-2799-4.

(10) Yaqoob, L.; Noor, T.; Iqbal, N. A Comprehensive and Critical Review of the Recent Progress in Electrocatalysts for the Ethanol Oxidation Reaction. *RSC Adv.* **2021**, *11* (27), 16768–16804. https://doi.org/10.1039/d1ra01841h.

(11) Shen, S. Y.; Zhao, T. S.; Xu, J. B. Carbon Supported PtRh Catalysts for Ethanol Oxidation in Alkaline Direct Ethanol Fuel Cell. *Int. J. Hydrogen Energy* **2010**, *35* (23), 12911–12917. https://doi.org/10.1016/j.ijhydene.2010.08.107.

(12) Takenaka, S.; Miyamoto, H.; Utsunomiya, Y.; Matsune, H.; Kishida, M. Catalytic Activity of Highly Durable Pt/CNT Catalysts Covered with Hydrophobic Silica Layers for the Oxygen Reduction Reaction in PEFCs. *J. Phys. Chem. C* **2014**, *118* (2), 774–783.

https://doi.org/10.1021/jp407928m.
(13) Robinson, J. E.; Labrador, N. Y.; Chen, H.; Sartor, B. E.; Esposito, D. V. Silicon Oxide-Encapsulated Platinum Thin Films as Highly Active Electrocatalysts for Carbon Monoxide and Methanol Oxidation. *ACS Catal.* **2018**, *8*, 11423–11434.
(14) Doyle, A. D.; Montoya, J. H.; Vojvodic, A. Improving Oxygen Electrochemistry through Nanoscopic Confinement. *ChemCatChem* **2015**, *7* (5). https://doi.org/10.1002/cctc.201402864.
(15) Perales-Rondón, J. V.; Herrero, E.; Feliu, J. M. Effects of the Anion Adsorption and PH on the Formic Acid Oxidation Reaction on Pt(111) Electrodes. *Electrochim. Acta* **2014**, *140*, 511–517. https://doi.org/10.1016/j.electacta.2014.06.057.
(16) Conway, B. E. Electrochemical At Noble Metals Oxide Film Formation As a Surface-Chemical Process. *Prog. Surf. Sci.* **1995**, *49* (95), 331–452. https://doi.org/Doi 10.1016/0079-6816(95)00040-6.
(17) Beatty, M. E. S.; Gillette, E. I.; Haley, A. T.; Esposito, D. V. Controlling the Relative Fluxes of Protons and Oxygen to Electrocatalytic Buried Interfaces with Tunable Silicon Oxide Overlayers. *ACS Appl. Energy Mater.* **2020**, *3* (12), 12338–12350. https://doi.org/10.1021/acsaem.0c02359.
(18) Rizo, R.; Arán-Ais, R. M.; Herrero, E. On the Oxidation Mechanism of C1-C2 Organic Molecules on Platinum. A Comparative Analysis. *Curr. Opin. Electrochem.* **2021**, *25*, 100648. https://doi.org/10.1016/j.coelec.2020.100648.
(19) Beatty, M. E. S.; Chen, H.; Labrador, N. Y.; Lee, B. J.; Esposito, D. V. Structure–Property Relationships Describing the Buried Interface between Silicon Oxide Overlayers and Electrocatalytic Platinum Thin Films. *J. Mater. Chem. A* **2018**, *6* (44), 22287–22300. https://doi.org/10.1039/C8TA06969G.
(20) Ouyang, M.; Yuan, C.; Muisener, R. J.; Boulares, a.; Koberstein, J. T. Conversion of Some Siloxane Polymers to Silicon Oxide by UV/Ozone Photochemical Processes. *Chem. Mater.* **2000**, *12* (29), 1591–1596. https://doi.org/10.1021/cm990770d.
(21) Ouyang, M.; Klemchuk, P. P.; Koberstein, J. T. Exploring the Effectiveness of SiOx Coatings in Protecting Polymers against Photo-Oxidation. *Polym. Degrad. Stab.* **2000**, *70* (2), 217–228. https://doi.org/10.1016/S0141-3910(00)00116-6.
(22) Jerkiewicz, G.; Vatankhah, G.; Lessard, J.; Soriaga, M. P.; Park, Y. S. Surface-Oxide Growth at Platinum Electrodes in Aqueous H2SO 4 Reexamination of Its Mechanism through Combined Cyclic-Voltammetry, Electrochemical Quartz-Crystal Nanobalance, and Auger Electron Spectroscopy Measurements. *Electrochim. Acta* **2004**, *49* (9–10), 1451–1459. https://doi.org/10.1016/j.electacta.2003.11.008.
(23) Mom, R.; Frevel, L.; Velasco-Vélez, J. J.; Plodinec, M.; Knop-Gericke, A.; Schlögl, R. The Oxidation of Platinum under Wet Conditions Observed by Electrochemical X-Ray Photoelectron Spectroscopy. *J. Am. Chem. Soc.* **2019**, *141* (16), 6537–6544. https://doi.org/10.1021/jacs.8b12284.
(24) Yuan, G.; Agiral, A.; Pellet, N.; Kim, W.; Frei, H. Inorganic Core-Shell Assemblies for Closing the Artificial Photosynthetic Cycle. *Faraday Discuss.* **2014**, *176*, 233–249. https://doi.org/10.1039/c4fd00150h.
(25) Batista, E. A.; Malpass, G. R. P.; Motheo, A. J.; Iwasita, T. New Insight into the Pathways of Methanol Oxidation. *Electrochem. commun.* **2003**, *5* (10), 843–846. https://doi.org/10.1016/j.elecom.2003.08.010.
(26) Topalov, A. A.; Cherevko, S.; Zeradjanin, A. R.; Meier, J. C.; Katsounaros, I.; Mayrhofer,

K. J. J. Towards a Comprehensive Understanding of Platinum Dissolution in Acidic Media. *Chem. Sci.* **2014**, *5* (2), 631–638. https://doi.org/10.1039/c3sc52411f.
(27) Housmans, T. H. M.; Wonders, A. H.; Koper, M. T. M. Structure Sensitivity of Methanol Electrooxidation Pathways on Platinum: An on-Line Electrochemical Mass Spectrometry Study. *J. Phys. Chem. B* **2006**, *110* (20), 10021–10031. https://doi.org/10.1021/jp055949s.
(28) Lović, J. The Kinetics and Mechanism of Methanol Oxidation on Pt and PtRu Catalysts in Alkaline and Acid Media. *J. Serbian Chem. Soc.* **2007**, *72* (7), 709–712. https://doi.org/10.2298/JSC0707709L.
(29) Figueiredo, M. C.; Sorsa, O.; Doan, N.; Pohjalainen, E.; Hildebrand, H.; Schmuki, P.; Wilson, B. P.; Kallio, T. Direct Alcohol Fuel Cells: Increasing Platinum Performance by Modification with Sp-Group Metals. *J. Power Sources* **2015**, *275*, 341–350. https://doi.org/10.1016/j.jpowsour.2014.11.034.
(30) Arán-Ais, R. M.; Vidal-Iglesias, F. J.; Farias, M. J. S.; Solla-Gullón, J.; Montiel, V.; Herrero, E.; Feliu, J. M. Understanding CO Oxidation Reaction on Platinum Nanoparticles. *J. Electroanal. Chem.* **2017**. https://doi.org/10.1016/j.jelechem.2016.09.031.
(31) Calderón-Cárdenas, A.; Hartl, F. W.; Gallas, J. A. C.; Varela, H. Modeling the Triple-Path Electro-Oxidation of Formic Acid on Platinum: Cyclic Voltammetry and Oscillations. *Catal. Today* **2019**. https://doi.org/10.1016/j.cattod.2019.04.054.
(32) Aslam, N. M.; Masdar, M. S.; Kamarudin, S. K.; Daud, W. R. W. Overview on Direct Formic Acid Fuel Cells (DFAFCs) as an Energy Sources. *APCBEE Procedia* **2012**, *3*, 33–39. https://doi.org/10.1016/j.apcbee.2012.06.042.
(33) Luque, G. C.; Gennero De Chialvo, M. R.; Chialvo, A. C. Kinetic Study of the Formic Acid Oxidation on Steady State Using a Flow Cell. *J. Electrochem. Soc.* **2017**, *164* (12), H748–H754. https://doi.org/10.1149/2.0581712jes.
(34) Chen, Y. X.; Heinen, M.; Jusys, Z.; Behm, R. J. Kinetics and Mechanism of the Electrooxidation of Formic Acid - Spectroelectrochemical Studies in a Flow Cell. *Angew. Chemie - Int. Ed.* **2006**, *45* (6), 981–985. https://doi.org/10.1002/anie.200502172.
(35) Wang, Y.; Qi, Y.; Zhang, D. New Mechanism of the Direct Pathway for Formic Acid Oxidation on Pd(111). *Comput. Theor. Chem.* **2014**, *1049*, 51–54. https://doi.org/10.1016/j.comptc.2014.09.020.
(36) Betts, A.; Briega-Martos, V.; Cuesta, A.; Herrero, E. Adsorbed Formate Is the Last Common Intermediate in the Dual-Path Mechanism of the Electrooxidation of Formic Acid. *ACS Catal.* **2020**, *10* (15), 8120–8130. https://doi.org/10.1021/acscatal.0c00791.
(37) Perales-Rondón, J. V.; Brimaud, S.; Solla-Gullón, J.; Herrero, E.; Jürgen Behm, R.; Feliu, J. M. Further Insights into the Formic Acid Oxidation Mechanism on Platinum: PH and Anion Adsorption Effects. *Electrochim. Acta* **2015**, *180*. https://doi.org/10.1016/j.electacta.2015.08.155.
(38) Chen, Y. X.; Ye, S.; Heinen, M.; Jusys, Z.; Osawa, M.; Behm, R. J. Application of In-Situ Attenuated Total Reflection-Fourier Transform Infrared Spectroscopy for the Understanding of Complex Reaction Mechanism and Kinetics: Formic Acid Oxidation on a Pt Film Electrode at Elevated Temperatures. *J. Phys. Chem. B* **2006**, *110* (19), 9534–9544. https://doi.org/10.1021/jp057463h.
(39) Chung, D. Y.; Lee, K. J.; Sung, Y. E. Methanol Electro-Oxidation on the Pt Surface: Revisiting the Cyclic Voltammetry Interpretation. *J. Phys. Chem. C* **2016**, *120* (17). https://doi.org/10.1021/acs.jpcc.5b12303.

(40) Folkman, S. J.; González-Cobos, J.; Giancola, S.; Sánchez-Molina, I.; Galán-Mascarós, J. R. Benchmarking Catalysts for Formic Acid/Formate Electrooxidation. *Molecules* **2021**, *26* (16). https://doi.org/10.3390/molecules26164756.
(41) Anderson, A. B.; Asiri, H. A. Reversible Potentials for Steps in Methanol and Formic Acid Oxidation to CO2; Adsorption Energies of Intermediates on the Ideal Electrocatalyst for Methanol Oxidation and CO2 Reduction. *Phys. Chem. Chem. Phys.* **2014**, *16* (22), 10587–10599. https://doi.org/10.1039/c3cp54837f.
(42) Hou, G.; Parrondo, J.; Ramani, V.; Prakash, J. Kinetic and Mechanistic Investigation of Methanol Oxidation on a Smooth Polycrystalline Pt Surface. *J. Electrochem. Soc.* **2014**, *161* (3), F252–F258. https://doi.org/10.1149/2.045403jes.
(43) Wang, J.; Zhang, B.; Guo, W.; Wang, L.; Chen, J.; Pan, H.; Sun, W. Toward Electrocatalytic Methanol Oxidation Reaction: Longstanding Debates and Emerging Catalysts. *Adv. Mater.* **2023**, *35* (26), 1–20. https://doi.org/10.1002/adma.202211099.
(44) Cohen, J. L.; Volpe, D. J.; Abruña, H. D. Electrochemical Determination of Activation Energies for Methanol Oxidation on Polycrystalline Platinum in Acidic and Alkaline Electrolytes. *Phys. Chem. Chem. Phys.* **2007**, *9* (1), 49–77. https://doi.org/10.1039/b612040g.
(45) Iwasita, T. Chapter 41 Methanol and CO Electrooxidation. **2003**, *2*.
(46) Ong, B. C.; Kamarudin, S. K.; Basri, S. Direct Liquid Fuel Cells: A Review. *International Journal of Hydrogen Energy*. 2017. https://doi.org/10.1016/j.ijhydene.2017.01.117.
(47) Flórez-Montaño, J.; García, G.; Guillén-Villafuerte, O.; Rodríguez, J. L.; Planes, G. A.; Pastor, E. Mechanism of Ethanol Electrooxidation on Mesoporous Pt Electrode in Acidic Medium Studied by a Novel Electrochemical Mass Spectrometry Set-Up. *Electrochim. Acta* **2016**, *209*. https://doi.org/10.1016/j.electacta.2016.05.070.
(48) Wang, H.; Löffler, T.; Baltruschat, H. Formation of Intermediates during Methanol Oxidation: A Quantitative DEMS Study. *J. Appl. Electrochem.* **2001**, *31* (7), 759–765. https://doi.org/10.1023/A:1017539411059.
(49) Mostafa, E.; Abd-El-Latif, A.-E.-A. A.; Ilsley, R.; Attard, G.; Baltruschat, H. Quantitative DEMS Study of Ethanol Oxidation: Effect of Surface Structure and Sn Surface Modification. *Phys. Chem. Chem. Phys.* **2012**, *14* (46), 16115. https://doi.org/10.1039/c2cp42520c.
(50) Khanipour, P.; Haschke, S.; Bachmann, J.; Mayrhofer, K. J. J.; Katsounaros, I. Electrooxidation of Saturated C1-C3 Primary Alcohols on Platinum: Potential-Resolved Product Analysis with Electrochemical Real-Time Mass Spectrometry (EC-RTMS). *Electrochim. Acta* **2019**, *315*, 67–74. https://doi.org/10.1016/j.electacta.2019.05.070.
(51) Batista, E. A.; Malpass, G. R. P.; Motheo, A. J.; Iwasita, T. New Mechanistic Aspects of Methanol Oxidation. *J. Electroanal. Chem.* **2004**, *571* (2), 273–282. https://doi.org/10.1016/j.jelechem.2004.05.016.
(52) Sorte, E. G.; Tong, Y. J. Interdigitated Metal Electrodes for High-Resolution in Situ Electrochemical NMR. *J. Electroanal. Chem.* **2016**, *769*, 1–4. https://doi.org/10.1016/j.jelechem.2016.03.003.
(53) Wang, F.; Jiang, Y.; Lawes, D. J.; Ball, G. E.; Zhou, C.; Liu, Z.; Amal, R. Analysis of the Promoted Activity and Molecular Mechanism of Hydrogen Production over Fine Au-Pt Alloyed TiO2 Photocatalysts. *ACS Catal.* **2015**, *5* (7), 3924–3931. https://doi.org/10.1021/acscatal.5b00623.
(54) Gomes, J. F.; Bergamaski, K.; Pinto, M. F. S.; Miranda, P. B. Reaction Intermediates of

Ethanol Electro-Oxidation on Platinum Investigated by SFG Spectroscopy. *J. Catal.* **2013**, *302*, 67–82. https://doi.org/10.1016/j.jcat.2013.02.024.
(55) Lee, M. J.; Kang, J. S.; Kang, Y. S.; Chung, D. Y.; Shin, H.; Ahn, C. Y.; Park, S.; Kim, M. J.; Kim, S.; Lee, K. S.; Sung, Y. E. Understanding the Bifunctional Effect for Removal of CO Poisoning: Blend of a Platinum Nanocatalyst and Hydrous Ruthenium Oxide as a Model System. *ACS Catal.* **2016**, *6* (4). https://doi.org/10.1021/acscatal.5b02580.
(56) Yuda, A.; Ashok, A.; Kumar, A. A Comprehensive and Critical Review on Recent Progress in Anode Catalyst for Methanol Oxidation Reaction. *Catal. Rev. - Sci. Eng.* **2020**. https://doi.org/10.1080/01614940.2020.1802811.
(57) Leung, L. W. H.; Weaver, M. J. Influence of Adsorbed Carbon Monoxide on the Electrocatalytic Oxidation of Simple Organic Molecules at Platinum and Palladium Electrodes in Acidic Solution: A Survey Using Real-Time FTIR Spectroscopy. *Langmuir* **1990**, *6* (2), 323–333. https://doi.org/10.1021/la00092a006.
(58) Mangoufis-Giasin, I.; Piqué, O.; Khanipour, P.; Mayrhofer, K. J. J.; Calle-Vallejo, F.; Katsounaros, I. Different Promoting Roles of Ruthenium for the Oxidation of Primary and Secondary Alcohols on PtRu Electrocatalysts. *J. Catal.* **2021**, *400*, 166–172. https://doi.org/10.1016/j.jcat.2021.05.028.
(59) Wang, H.; Abruña, H. D. New Insights into Methanol and Formic Acid Electro-Oxidation on Pt: Simultaneous DEMS and ATR-SEIRAS Study under Well-Defined Flow Conditions and Simulations of CO Spectra. *J. Chem. Phys.* **2022**, *156* (3), 034703. https://doi.org/10.1063/5.0071463.
(60) Gómez-Marín, A. M.; Feliu, J. M. Pt(1 1 1) Surface Disorder Kinetics in Perchloric Acid Solutions and the Influence of Specific Anion Adsorption. *Electrochim. Acta* **2012**, *82*, 558–569. https://doi.org/10.1016/j.electacta.2012.04.066.
(61) Tripković, A. V.; Gojković, S. L.; Popović, K. D.; Lović, J. D. Methanol Oxidation at Platinum Electrodes in Acid Solution: Comparison between Model and Real Catalysts. *J. Serbian Chem. Soc.* **2006**, *71* (12), 1333–1343. https://doi.org/10.2298/JSC0612333T.
(62) Ferre-Vilaplana, A.; Perales-Rondón, J. V.; Buso-Rogero, C.; Feliu, J. M.; Herrero, E. Formic Acid Oxidation on Platinum Electrodes: A Detailed Mechanism Supported by Experiments and Calculations on Well-Defined Surfaces. *J. Mater. Chem. A* **2017**, *5* (41). https://doi.org/10.1039/c7ta07116g.
(63) Ferre-Vilaplana, A.; Perales-Rondón, J. V.; Feliu, J. M.; Herrero, E. Understanding the Effect of the Adatoms in the Formic Acid Oxidation Mechanism on Pt(111) Electrodes. *ACS Catal.* **2015**, *5* (2). https://doi.org/10.1021/cs501729j.
(64) Mai, P. T.; Haze, A.; Chiku, M.; Higuchi, E.; Inoue, H. Ethanol Oxidation Reaction on Tandem Pt/Rh/SnOx Catalyst. *Catalysts* **2017**, *7* (9). https://doi.org/10.3390/catal7090246.
(65) Lai, S. C. S.; Lebedeva, N. P.; Housmans, T. H. M.; Koper, M. T. M. Mechanisms of Carbon Monoxide and Methanol Oxidation at Single-Crystal Electrodes. *Top. Catal.* **2007**, *46* (3–4), 320–333. https://doi.org/10.1007/s11244-007-9010-y.
(66) Lai, S. C. S.; Koper, M. T. M. The Influence of Surface Structure on Selectivity in the Ethanol Electro-Oxidation Reaction on Platinum. *J. Phys. Chem. Lett.* **2010**, *1* (7), 1122–1125. https://doi.org/10.1021/jz100272f.
(67) Herrero, E.; Franaszczuk, K.; Wieckowski, A. Electrochemistry of Methanol at Low Index Crystal Planes of Platinum. An Integrated Voltammetric and Chronoamperometric Study. *J. Phys. Chem.* **1994**, *98* (19), 5074–5083. https://doi.org/10.1021/j100070a022.

(68) Esposito, D. V.; Giulimondi, V.; Koper, M. Design Principles for Oxide-Encapsulated Electrocatalysts. In *Ultrathin Oxide Layers for Solar, Electrocatalytic, and Thermal Catalytic Systems*; 2020; p Under Editorial Review.
(69) Li, H.; Xiao, J.; Fu, Q.; Bao, X. Confined Catalysis under Two-Dimensional Materials. *Proc. Natl. Acad. Sci.* **2017**, *114* (23), 5930–5934. https://doi.org/10.1073/pnas.1701280114.
(70) Andronescu, C.; Masa, J.; Tilley, R. D.; Gooding, J. J.; Schuhmann, W. Electrocatalysis in Confined Space. *Curr. Opin. Electrochem.* **2021**, *25*, 100644. https://doi.org/10.1016/j.coelec.2020.100644.
(71) Han, X.; Gao, Q.; Yan, Z.; Ji, M.; Long, C.; Zhu, H. Electrocatalysis in Confined Spaces: Interplay between Well-Defined Materials and the Microenvironment. *Nanoscale* **2021**, *13* (3), 1515–1528. https://doi.org/10.1039/d0nr08237f.
(72) Mitschke, B.; Turberg, M.; List, B. Confinement as a Unifying Element in Selective Catalysis. *Chem* **2020**, *6* (10), 2515–2532. https://doi.org/10.1016/j.chempr.2020.09.007.
(73) Dong, B.; Pei, Y.; Mansour, N.; Lu, X.; Yang, K.; Huang, W.; Fang, N. Deciphering Nanoconfinement Effects on Molecular Orientation and Reaction Intermediate by Single Molecule Imaging. *Nat. Commun.* **2019**, *10* (1), 1–6. https://doi.org/10.1038/s41467-019-12799-x.
(74) Mouarrawis, V.; Plessius, R.; van der Vlugt, J. I.; Reek, J. N. H. Confinement Effects in Catalysis Using Well-Defined Materials and Cages. *Front. Chem.* **2018**, *6* (DEC), 1–20. https://doi.org/10.3389/fchem.2018.00623.
(75) Wang, P.; Steinmann, S. N.; Fu, G.; Michel, C.; Sautet, P. Key Role of Anionic Doping for H2 Production from Formic Acid on Pd(111). *ACS Catal.* **2017**, *7* (3), 1955–1959. https://doi.org/10.1021/acscatal.6b03544.
(76) Scaranto, J.; Mavrikakis, M. HCOOH Decomposition on Pt(111): A DFT Study. *Surf. Sci.* **2016**, *648*, 201–211. https://doi.org/10.1016/j.susc.2015.09.023.
(77) Gao, W.; Keith, J. A.; Anton, J.; Jacob, T. Theoretical Elucidation of the Competitive Electro-Oxidation Mechanisms of Formic Acid on Pt(111). *J. Am. Chem. Soc.* **2010**, *132* (51), 18377–18385. https://doi.org/10.1021/ja1083317.
(78) Clavilier, J.; Parsons, R.; Durand, R.; Lamy, C.; Leger, J. M. Formic Acid Oxidation on Single Crystal Platinum Electrodes. Comparison with Polycrystalline Platinum. *J. Electroanal. Chem.* **1981**, *124* (1–2), 321–326. https://doi.org/10.1016/S0022-0728(81)80311-7.
(79) Marushkevich, K.; Khriachtchev, L.; Räsänen, M. Hydrogen Bonding between Formic Acid and Water: Complete Stabilization of the Intrinsically Unstable Conformer. *J. Phys. Chem. A* **2007**, *111* (11), 2040–2042. https://doi.org/10.1021/jp070363m.
(80) Zhong, W.; Wang, R.; Zhang, D.; Liu, C. Theoretical Study of the Oxidation of Formic Acid on the PtAu(111) Surface in the Continuum Water Solution Phase. *J. Phys. Chem. C* **2012**, *116* (45), 24143–24150. https://doi.org/10.1021/jp307923x.
(81) Chen, B. W. J.; Mavrikakis, M. Formic Acid: A Hydrogen-Bonding Cocatalyst for Formate Decomposition. *ACS Catal.* **2020**, *10* (19), 10812–10825. https://doi.org/10.1021/acscatal.0c02902.
(82) Lockwood, G. K.; Garofalini, S. H. Bridging Oxygen as a Site for Proton Adsorption on the Vitreous Silica Surface. *J. Chem. Phys.* **2009**, *131* (7), 074703. https://doi.org/10.1063/1.3205946.
(83) Goettmann, F.; Sanchez, C. How Does Confinement Affect the Catalytic Activity of

Mesoporous Materials? *J. Mater. Chem.* **2007**, *17* (1), 24–30. https://doi.org/10.1039/b608748p.
(84) Takenaka, S.; Miyazaki, T.; Matsune, H.; Kishida, M. Highly Active and Durable Silica-Coated Pt Cathode Catalysts for Polymer Electrolyte Fuel Cells: Control of Micropore Structures in Silica Layers. *Catal. Sci. Technol.* **2015**, *5* (2), 1133–1142. https://doi.org/10.1039/c4cy01301h.
(85) Ouyang, M.; Muisener, R. J.; Boulares, A.; Koberstein, J. T. UV-Ozone Induced Growth of a SiO(x) Surface Layer on a Cross-Linked Polysiloxane Film: Characterization and Gas Separation Properties. *J. Memb. Sci.* **2000**, *177* (1–2), 177–187. https://doi.org/10.1016/S0376-7388(00)00471-3.
(86) Labrador, N. Y.; Songcuan, E. L.; De Silva, C.; Chen, H.; Kurdziel, S. J.; Ramachandran, R. K.; Detavernier, C.; Esposito, D. V. Hydrogen Evolution at the Buried Interface between Pt Thin Films and Silicon Oxide Nanomembranes. *ACS Catal.* **2018**, *8* (3), 1767–1778. https://doi.org/10.1021/acscatal.7b02668.
(87) Peng, Z.; Wang, H.; Zhou, L.; Wang, Y.; Gao, J.; Liu, G.; Redfern, S. A. T.; Feng, X.; Lu, S.; Li, B.; Liu, Z. Hollow Carbon Shells Enhanced by Confined Ruthenium as Cost-Efficient and Superior Catalysts for the Alkaline Hydrogen Evolution Reaction. *J. Mater. Chem. A* **2019**, *7* (12), 6676–6685. https://doi.org/10.1039/c8ta09136f.
(88) Zhou, T. Y.; Auer, B.; Lee, S. J.; Telfer, S. G. Catalysts Confined in Programmed Framework Pores Enable New Transformations and Tune Reaction Efficiency and Selectivity. *J. Am. Chem. Soc.* **2019**, *141* (4), 1577–1582. https://doi.org/10.1021/jacs.8b11221.
(89) Van der Perre, S.; Van Assche, T.; Bozbiyik, B.; Lannoeye, J.; De Vos, D. E.; Baron, G. V.; Denayer, J. F. M. Adsorptive Characterization of the ZIF-68 Metal-Organic Framework: A Complex Structure with Amphiphilic Properties. *Langmuir* **2014**, *30* (28), 8416–8424. https://doi.org/10.1021/la501594t.
(90) Cremers, C.; Bayer, D.; Kintzel, B.; Joos, M.; Jung, F.; Krausa, M.; Tübke, J. Oxidation of Alcohols in Acidic and Alkaline Environments. *ECS Trans.* **2008**, *16* (2), 1263–1273. https://doi.org/10.1149/1.2981967.
(91) Han, Z.; Kortlever, R.; Chen, H. Y.; Peters, J. C.; Agapie, T. CO2 Reduction Selective for C≥2 Products on Polycrystalline Copper with N-Substituted Pyridinium Additives. *ACS Cent. Sci.* **2017**, *3* (8), 853–859. https://doi.org/10.1021/acscentsci.7b00180.
(92) Thevenon, A.; Rosas-Hernández, A.; Peters, J. C.; Agapie, T. In-Situ Nanostructuring and Stabilization of Polycrystalline Copper by an Organic Salt Additive Promotes Electrocatalytic CO2 Reduction to Ethylene. *Angew. Chemie - Int. Ed.* **2019**, *58* (47), 16952–16958. https://doi.org/10.1002/anie.201907935.
(93) Buckley, A. K.; Lee, M.; Cheng, T.; Kazantsev, R. V.; Larson, D. M.; Goddard, W. A.; Toste, F. D.; Toma, F. M. Electrocatalysis at Organic-Metal Interfaces: Identification of Structure-Reactivity Relationships for Co2 Reduction at Modified Cu Surfaces. *J. Am. Chem. Soc.* **2019**, *141* (18), 7355–7364. https://doi.org/10.1021/jacs.8b13655.